Fall 2023

Interfacial Thermomechanical Behavior of Hybrid Carbon Fibers

Sriraj Srihari
Embry-Riddle Aeronautical University, sriharis@my.erau.edu

INTERFACIAL THERMOMECHANICAL BEHAVIOR OF HYBRID CARBON FIBERS

By

Sriraj Srihari

A Thesis Submitted to the Faculty of Embry-Riddle Aeronautical University

In Partial Fulfillment of the Requirements for the Degree of

Master of Science in Aerospace Engineering

December 2023

Embry-Riddle Aeronautical University

Daytona Beach, Florida

INTERFACIAL THERMOMECHANICAL BEHAVIOR OF HYBRID CARBON FIBERS

By

Sriraj Srihari

This Thesis was prepared under the direction of the candidate's Thesis Committee Chair, Dr. Sirish Namilae, Department of Aerospace Engineering, and has been approved by the members of the Thesis Committee. It was submitted to the Office of the Senior Vice President for Academic Affairs and Provost, and was accepted in the partial fulfillment of the requirements for the Degree of Master of Science in Aerospace Engineering.

THESIS COMMITTEE

Sirish Namilae Digitally signed by Sirish Namilae Date: 2023.11.30 19:18:41 -05'00'

Chair, Dr. Sirish Namilae

Member, Dr. Alberto Mello

Member, Dr. Mandar Kulkarni

Graduate Program Coordinator, Dr. Hever Moncayo

Date

Dean of the College of Engineering, Dr. James W. Gregory

Date

Associate Provost of Academic Support, Dr. Kelly Austin

Date

ACKNOWLEDGEMENTS

First, I would like to give my heartfelt appreciation for my advisor Dr. Sirish Namilae. From the start, he worked with me to build my foundations in research then gave me a task that well suited my abilities. His mentorship and assistance proved invaluable in my masters journey. I would also like to thank my other committee members Dr. Alberto Mello and Dr. Mandar Kulkarni for their advice and help throughout this research.

Thank you to all the students in the composites and structures labs as well. I have made many valuable friends and their constant presence and good memories made this endeavour much more enjoyable. A special thanks to Marie and Derek; without them I would not have many samples to work with or knowledge about the various lab's tools and equipment.

I'd like to also thank my family and friends back home. Their presence in my life provided a good escape from the stresses of college.

Finally, I appreciate funding from NSF grants 2018375 and 2001038 in supporting my research.

ABSTRACT

The carbon fiber/epoxy interface is of great importance in composite design due to its load transfer mechanisms from the weak epoxy to the stronger fiber. Improving the strength of the interface reduces the risk of failure at the interface and improves the load transfer to the fiber. In this study, two types of nano-species ZnO nanowires and nickel-based metal organic frameworks were grown on carbon fibers to improve the interfaces.

The interfacial mechanics of the enhanced fibers are evaluated using nanoindentation studies. Composite samples with Aeropoxy matrix and vertically aligned fibers are fabricated for this purpose. A Bruker TI-980 TriboIndenter is used to perform single-fiber push-in tests to analyze the interfacial behavior. The load-displacement curves of these push-in tests denote a clear nonlinearity where debonding occurs, and the debonding loads are used to calculate interfacial shear stress. A 15-20% improvement in interfacial strength was observed with the fiber modification. Along with that, modulus mapping techniques allow for the analysis of the change in moduli along the interface. In conjunction with mechanical analysis, chemical and hydrodynamic perspectives are also investigated for additional reasoning as to why nano-species surface modification positively affects the fiber/matrix interface. These perspectives show that the increase in roughness on the fiber's surface, increase in surface free energy, and decrease in interfacial tension of the nano-species increases the wettability of the epoxy onto the fiber's surface. The combined mechanical, chemical, and hydrodynamic analyses lead to the conclusion that the growth of these nano-species enhances the interfacial properties of the carbon fibers and opens promising possibilities for multifunctional applications by harnessing the properties of the nanomaterials.

TABLE OF CONTENTS

ACKNOWLEDGEMENTS i

ABSTRACT ii

TABLE OF CONTENTS iii

LIST OF FIGURES v

LIST OF TABLES vii

NOMENCLATURE viii

1 Introduction 1

1.1 Thesis Objectives 2

2 Review of the Relevant Literature 4

2.1 Interface Modification – Hybrid Materials 4

2.2 Mechanisms Affecting Interfacial Strength in Hybrid Fibers 6

2.3 ZnO Crystals & Growth Methods 8

2.4 MOF & Growth Methods 10

2.5 Methods for Measuring Interfacial Properties 11

2.6 Nanoindentation Based Single Fiber Push-In Testing 14

2.7 Modeling Approaches for Interfaces 15

3 Experimental Approach 18

3.1 Materials 18

3.2 Equipment 18

3.3 Nano-Species Growth Procedures 21

3.3.1 ZnO Growth Procedure 22

3.3.2 MOF Growth Procedure 23
3.4 Microstructural Characterization 23
3.5 Composite Sample Preparation 24
3.6 Nanoindentation 25
3.6.1 Low Load Scanning 27
3.6.2 Modulus Mapping 28
3.6.3 Low Load Indentation 28
3.6.4 High Load Indentation 29
4 Results and Discussion 30
4.1 Microstructural Analysis 30
4.2 Nanoindentation 37
4.2.1 Low Load Indentation 37
4.2.2 Low Load xSol 41
4.2.3 High Load Indentation 44
4.2.4 Modulus Mapping 50
4.3 Wetting Considerations 53
4.4 Discussion 55
5 Conclusions and Future Work 59
5.1 Future Work 59
6 REFERENCES 62

LIST OF FIGURES

Figure **Page**

Figure 1.1 Schematic of (a) Good Bonding, and (b) Poor Bonding in an FRP 2

Figure 2.1 ZnO Growth on Carbon Fiber 9

Figure 2.2 MOF Growth on Carbon Fiber 10

Figure 3.1 Drying Oven for Composite Samples 19

Figure 3.2 Grinder-Polisher Machine 19

Figure 3.3 Grinding and Polishing Pads, and Alumina Polishing Suspensions 20

Figure 3.4 FEI Quanta 650 SEM 20

Figure 3.5 TI-980 NanoIndenter 21

Figure 3.6 Fiber Desizing Tube Furnace 22

Figure 3.7 Composite Curing Moat with Fibers Inside 24

Figure 3.8 Initially cut sample (left), and sample after grinding and polishing (right) 25

Figure 3.9 Sample Surface Under Optics 27

Figure 4.1 As-Is Fiber 30

Figure 4.2 As-Is Fiber with Diameter Measured 31

Figure 4.3 ZnO Growth on Single Fiber 31

Figure 4.4 ZnO Fiber with Measured Diameters 32

Figure 4.5 ZnO Fiber with Measured Height 33

Figure 4.6 ZnO Fiber with Measured Crystal Spacing 33

Figure 4.7 MOF Growth on Carbon Fibers [47] 34

Figure 4.8 MOF Fiber with Measured Diameters 35

Figure 4.9 MOF Fiber with Measured Wall Width 35

Figure 4.10 MOF Fiber with Measured Pore Width 36

Figure 4.11 Comparison Load-Displacement Curves from Low Load Indentation 37

Figure **Page**

Figure 4.12 As-Is Representative Curves 38

Figure 4.13 ZnO Representative Curves 38

Figure 4.14 MOF Representative Curves 39

Figure 4.15 Epoxy Representative Curves 39

Figure 4.16 SPM Scans on (a) As-Is, (b) ZnO, (c) MOF, and (d) Epoxy 41

Figure 4.17 As-Is xSol Comparison 42

Figure 4.18 ZnO xSol Comparison 42

Figure 4.19 MOF xSol Comparison 43

Figure 4.20 Epoxy xSol Comparison 43

Figure 4.21 xSol SPM profiles for (a) As-Is Fiber, (b) ZnO Fiber, and (c) MOF Fiber 44

Figure 4.22 Load-Displacement Curves for High Load 45

Figure 4.23 As-Is High Load Curves with Debonding Loads Highlighted 45

Figure 4.24 ZnO High Load Curves with Debonding Loads Highlighted 46

Figure 4.25 MOF High Load Curves with Debonding Highlighted 46

Figure 4.26 Results of Increasing Load Experiment 47

Figure 4.27 SPM Scans of (a) 15 mN, (b) 30 mN, (c) 40 mN 48

Figure 4.28 Schematic of High Load Indentation 48

Figure 4.29 Modulus Mapping Results Showing Topology (top row), Storage Modulus (middle row), and Loss Modulus (bottom row) for each fiber 51

Figure 4.30 (a) Storage Modulus Profiles. (b) Loss Modulus Profiles 52

Figure 4.31 Snapshot of Matrix-Fiber Transition Region 52

Figure 4.32 Schematic of Wenzel and Cassie-Baxter Wetting Models 54

Figure 5.1 FEA Vertical Deformation Result 61

Figure 5.2 Comparison between Abaqus Data and Nanoindentation Data 61

LIST OF TABLES

Table **Page**

Table 4.1 Comparison of Indentation Data at Room Temperature..... 40

Table 4.2 Comparison of Indentation Data at Elevated Temperature 44

Table 4.3 High Load Interfacial Strength Data..... 50

NOMENCLATURE

(C)FRP	*(*Carbon) Fiber Reinforced Plastic
CNT	Carbon Nanotubes
ZnO	Zinc Oxide
MOF	Metal Organic Frameworks
SEM	Scanning Electron Microscopy
CVD	Chemical Vapor Deposition
SPM	Scanning Probe Microscopy
DI	Deionized Water
τ	Interfacial Shear Stress
P	Debonding Load
D	Fiber Diameter
t	Thickness of Sample

1 Introduction

Composite materials are those that consist of two or more macroscopically different materials that are combined together to create a third material with improved properties than the first two [1]. These materials are widely used today in a fiber reinforced polymer matrix (FRP) format, featuring high strength to weight ratios; they are used in a variety of industries such as automotive, sporting, and aerospace. One example of an FRP in aerospace is with Airbus, where the A350 aircraft has an airframe consisting of 52% carbon fiber reinforced plastic (CFRP) [2]. CFRPs consist of two parts – carbon fiber and matrix, with the carbon fiber being the reinforcing agent of the matrix. The material properties of the two materials are different, with the carbon fibers having much greater stiffness and strength than the matrix. With this combination of two materials, there is a region that connects fiber and matrix called the interface.

The interface region of the matrix and fiber is of great importance in composite design as that is the interaction region between the two materials. The interface region of carbon fiber/epoxy composites is usually defined as the chemically bonded region between the carbon fiber and the matrix [3]. The role of the interface is to facilitate the load transfer from the matrix to the fiber during some external loading [4]; this would affect the shear and delamination resistances, compressive strength, and fatigue endurance of the CFRP [5]. However, these benefits are only effective if there is effective bonding between the matrix and the fiber. An example of this is shown in Figure 1.1. Figure 1.1a is an example of a composite with strong bonding. This would result in effective load transfer between the matrix and fiber. Figure 1.1b is an example of poor bonding, in this case no bonding. If there is poor/no bonding between the fiber and matrix, then there can be little/no load transfer. If the interfacial strength is low, the system acts as if the fiber is not present, resulting in a composite with a hole in the middle.

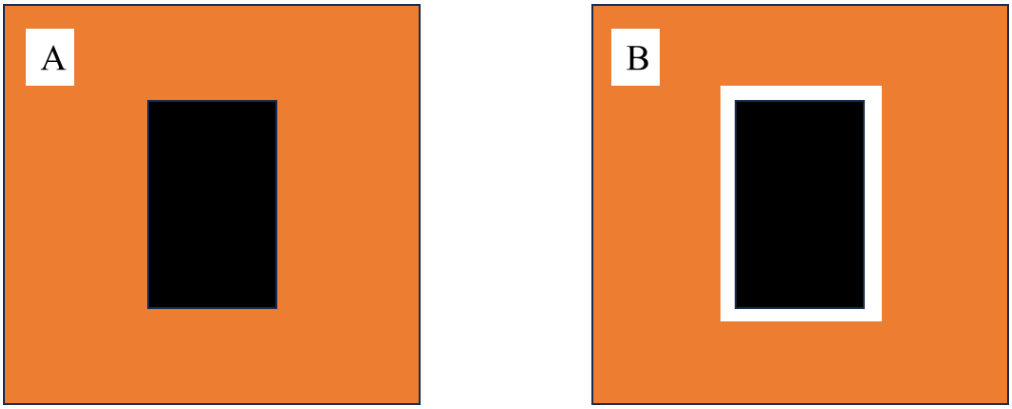

Figure 1.1 Schematic of (a) Good Bonding, and (b) Poor Bonding in an FRP

Despite the high stiffness and high strengths of standard carbon fiber, they do not exhibit strong interfacial bonding. This is because of the chemical inertness, stable non-polar structure, and low friction of graphitic surfaces of the fibers. Methods like sizing are often employed to modify these aspects and improve interfacial strength in commercial fibers. An active area of research involves methods for carbon fiber surface modification in order to improve the interfacial bonding between the fiber and epoxy, e.g., in-situ growth of nanomaterials.

1.1 Thesis Objectives

The objectives of the thesis are as follows:

Objective 1: Understanding Nano-Species Fiber Interface Modification

Gain a comprehensive understanding of how nano-species fiber interface modification impacts the fiber/matrix interface at a nanoscale, single-fiber level, by exploring the theoretical aspects of nanoscale modification to establish foundational knowledge. This is done by investigating different modification methods to comprehend the various mechanisms enhancing fiber modification and mechanical performance focusing on zinc oxide nanocrystals and metal organic frameworks, their synthesis and characterization.

Objective 2: Experimental Analysis Of The Fiber Matrix Interface At Nanoscale

The second objective is to develop methods to accurately measure interface properties at the nanoscale level using a nanoindenter. The Bruker TI-980 nanoindenter system is used to characterize the interface and determine relevant parameters. This is done using a variety of indentation and imaging methods.

Objective 3: Comparison Of Different Interfacial Modification Methods Using Modulus Mapping

The third objective is to use modulus mapping to capture the change in moduli through the composite interface. This process is performed using the nanoindenter system and will allow the analysis of modulus through the matrix, fiber, and interface.

The thesis integrates the acquired knowledge from understanding, experimentation, and analysis to enhance comprehension of carbon fiber surface modification through nano-species growth.

2 Review of the Relevant Literature

Carbon Fiber Reinforced Plastics (CFRPs) are widely used in a variety of industries, including aerospace. As CFRP performance hinges on the effective load transfer between matrix and fiber, the fiber/matrix interface is an important parameter to keep track of. Normally, carbon fibers have a graphitic build with a stable surface, which results in poor interfacial bonding. To combat this, researchers have been looking for ways to improve the bonding between fiber and matrix by modifying the surface of the carbon fibers.

2.1 Interface Modification – Hybrid Materials

There are many studies that suggest using nanoscale materials like CNTs as a secondary form of reinforcement in the matrix [6-8], showing improvements in various mechanical and electrical properties. However, there are some challenges as well. One challenge is achieving a uniform distribution of the nano-species, which is important to not have matrix-rich areas that are weak compared to the rest of the sample [9].

A different method is to modify the surface of the fiber such that the reinforcement material is in the interface between fiber and epoxy. Various methods exist for modifying the surface of carbon fibers including wet, oxidative, or nano-species [10-11]. The goals of these methods are to benefit the fiber/matrix interface by increasing wettability, increasing the number of active sites on the fiber's surface, creating porosity through which the matrix can embed itself in, and more [12].

Wet methods are a common source of surface modification, with sizing being the most well-known of them. Sizing is a polymeric coating applied to the surface of the fiber during manufacture; it protects the fibers from fraying and keeps them safe from the outside elements. Dry methods feature various methodologies such as ozone treatment or plasma surface treatment.

One type of dry modification is nickel coating, where nickel plates are coated on the surface of the fiber; this leads to increased interfacial adhesion or increased fracture toughness [13].

This research features nano-species modification. The goal of this method is to employ various ceramic or metallic structured species on the surface of the fiber, for example nanoparticles, nanowires, or nanotubes. The benefits of the nano-species are that they increase the surface area of the fibers, introduce functional groups on the fiber's surface, and promote mechanical interlocking/tethering. One well known example of nano-species surface modification is with carbon nanotubes (CNTs) [14]. Nano-species can be placed on the surface of fibers using a variety of methods: growth, deposition, grafting, and more. An example of nano-species growth is with Liu et al., wherein they grow carbon nano coils on the surface of carbon fiber [15].

The physical and chemical nature of these various nano-species placement methods allows for uniform coating of the nano-species, as well as stronger adhesion to the matrix. These hybrid carbon fiber composites lead to improvements in tensile strength and interfacial shear strength [16-18]. These improvements depend on the type of nano-species used and placement method, but overall nano-species tend to improve the interfacial bond between fiber and matrix. Along with increased mechanical performance, nano-species create a multifunctionality aspect of composites. Certain nano-species can be used to create a secondary benefit for a composite. For example, Sharma and Kar developed a CNT coated carbon fiber filament for luminescent lightbulbs [19], Malakooti et al. used a Zinc Oxide Nanowire (ZnO) interface to create composites with embedded energy harvesting capabilities [20], and Deka et al. used a ZnO woven composite to create a more effective structural supercapacitor [21]. Much potential lies in the future of these nano-species incorporated hybrid composites, through both increased strength in a structural capacity and also its use in various engineering applications.

2.2 Mechanisms Affecting Interfacial Strength in Hybrid Fibers

Interfacial modification affects the fiber/matrix interface through various means: increasing surface area, creating mechanical tethering and nanoscale Z-pinning to the epoxy, promoting chemical interaction on the surface of the fiber, and increases wetting. Potentially, one downside of the modification is fiber degradation. In a good composite design, all these parameters would need to be balanced to improve the strength but can potentially reduce interface strength as well.

Yuan et al. shows that interface modification increases the surface area of a carbon fiber [22]. They modified the fiber's surface with various coupling agent molecules and used a parameter known as the specific surface area to compare the effects of these coupling agents. They found that the specific area for the modified fiber was almost 3 times more than the untreated fiber. This increased surface area also assists in thermal performance as well. Due to the increase in surface area, heat has more area to transfer in and out of the interface. Wickramasingha et al. used an acrylate derived polymer surface coating on carbon fibers to test tensile strength and modulus at both room temperature and at 600 °C. They found that at room temperature, tensile strength increased by 23.7% and modulus increased by 8%; however, at elevated temperatures, the tensile strength increase dropped to 20% and modulus increase dropped to 7% [23]. Their experimental results suggest that the surface modification provides a protection layer against thermal effects, maintaining the integrity of the interface. Interfacial shear strength also had a drop off from 208% at room temperature to 84% at elevated temperature, but this was still an increase from an unmodified state. The increased surface area would also affect thermal performance during cure. Kumar et al. used a thermal camera to monitor the cooling rate of a 2-layer composite with and without a ZnO nanowire coating. They found that the ZnO growth increased the cooling rate of the composite, even starting cooling from a decreased temperature than with the bare carbon fibers

[24]. They show that the increased surface area (500% increase from initial) promotes heat transfer in and out of the fiber resulting in faster cooling and a high epoxy degree of cure at the interface.

Nanoscale modification also creates a mechanical tethering effect between fiber and epoxy. Essentially, the fiber modification would act as a hook or tether, latching onto the epoxy with greater strength than the bare carbon fibers. This would result in a stronger bond between fiber and epoxy, having implications in mechanical performance. As the interface is the mechanism for various mechanical effects like shear or fatigue effects, this tethering positively affects variables such as fatigue strength or shear strength. Yang et al. used a silane coupling agent modification method to create reinforced fiber composites. They found that the interlaminar shear stress (affects delamination) increased by 42% [25]. SEM imaging after interlaminar shear testing showed that the matrix had very poor bonding to the fiber in its bare state; however, the modified fiber showed continuity in the matrix, with the fiber completely being embedded in the matrix. Furthermore, there were no observed micro-cracks in the interface. Eyckens et al. showed this tethering effect through both physical testing and molecular dynamics simulations [26]. Their study used amphiphilic molecules grafted on the surface of the fiber to improve the interface. The design of the molecules was such that the hydrophilic side of the molecule was attached to the fiber; the idea is that the hydrophilic side would interact with the epoxy, using the attraction of the molecule to bring more epoxy closer to the surface of the fiber. The physical testing of the composite found that the interfacial shear strength increased by 276%. The molecular dynamics simulation of the interface showed that the molecules acted as hooks in the epoxy that increased the interfacial strength and adhesion of the fiber/matrix interface.

Wetting is a measure of how well the epoxy bonds to the fiber's surface. Normally, carbon fibers do not have good wettability as they are smooth and inert. This leads to reduced mechanical

performance. Xu et al. modified carbon fibers using acrylic acid to experimentally look at the effects of modification on wettability [27]. Firstly, they found that the acid modification increased the total surface free energy of the fiber from 42.2 mJm^{-2} to 49.8 mJm^{-2}. They also analyzed surface morphologies of interlaminar fracture surfaces to find that the untreated fibers featured fiber debonding as a main failure point, but the treated fibers had little to no debonding and more matrix failure. Their results are important as if the fiber has more surface free energy than the matrix, then the fiber/matrix wetting will be stronger and more effective. The nanoscale modification method chosen should then aim to increase the surface energy of the fiber to be more than that of the epoxy, in order to promote greater adhesion and resulting increase in mechanical performance.

Processing also plays a key role in the health of the nano-species and fiber. High temperature based methods can be used like catalytic chemical vapor deposition to avoid this, but then the high temperature regimes (700 – 1200 °C) would potentially result in fiber degradation [28]. Similar thought would need to be put into chemical based methods as well, as too much acid may also lead to degradation of fibers. To combat some of these challenges, research has also looked into optimizing growth conditions for various methods like CVD in order to minimize or eliminate fiber degradation [29].

2.3 ZnO Crystals & Growth Methods

One example of a nano-species is zinc oxide nanowire (ZnO). Zinc oxide is a ceramic material with a wurtzite (hexagonal) crystal structure [30]. It is a material of great importance as it has piezoelectric, pyroelectric, and semiconducting abilities [31]. Due to this, ZnO can be used in a variety of applications such as in sensors and actuators [32] and solar cells [33]. ZnO can take many nanoscale forms: rods, combs, rings, and more are all possible by modifying growth parameters such as time, temperature, and pressure [34]. Figure 2.1 shows an example of ZnO growth on carbon fibers.

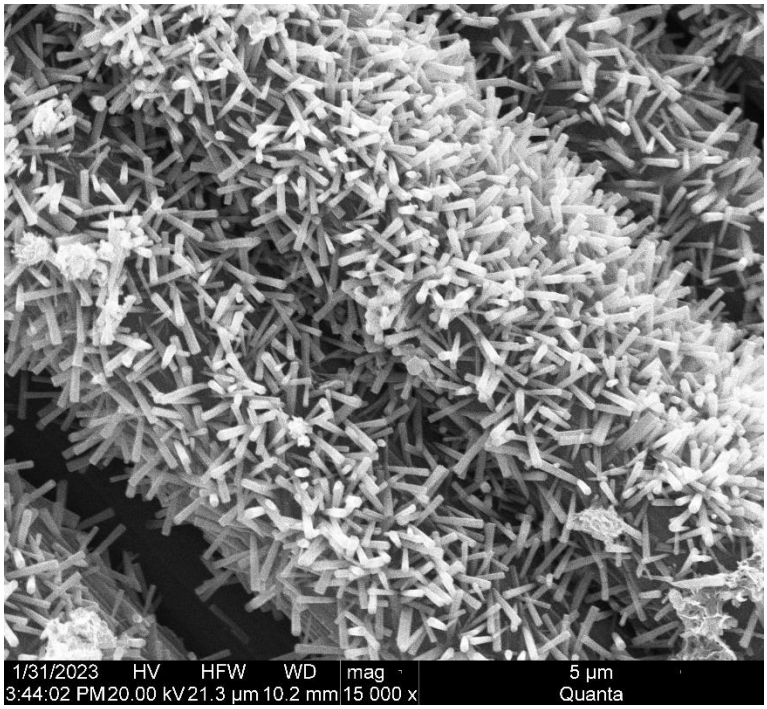

Figure 2.1 ZnO Growth on Carbon Fiber

There are a few ways to grow ZnO nanostructures on materials. Some include chemical vapor deposition, lithography, and hydrothermal seed layer based methods [35]. One unique way of ZnO growth is a combination of hydrothermal and atomic layer deposition (ALD). This method uses ALD to deposit zinc and oxygen onto the surface of the fiber, then a hydrothermal process to stimulate growth. This process results in a uniform growth on the fiber's surface [36]. The most common method of ZnO growth on carbon fibers is with a hydrothermal process. This process uses various aqueous solutions for the fibers to soak in. There would be seeding solutions and growth solutions, and for each step the fibers would be placed in these solutions such that the particles in the solutions would be bonded to the fiber (using heat as a catalyst). Various studies show that hydrothermal growth results in uniform ZnO growth [20,37], and there are even studies that show that the grown ZnO positively affects the interface strength. For example, Galan et al.

grew ZnO with various morphologies (variation of length and diameter) and found that interfacial shear strength would increase up to 228% from standard [38].

2.4 MOF & Growth Methods

Another example of nano-species are metal organic frameworks (MOFs). MOFs are a metallic material consisting of a positive metallic ion that is chained together with an organic linker molecule. This is repeated in a crystalline fashion to create highly porous materials [39]. Along with the benefit of high porosity, the metallic ion of choice is flexible. Many options for metallic ions can be used such as gold, nickel, or silver. Figure 2.2 shows a micrograph of MOF nanostructures on the surface of carbon fibers.

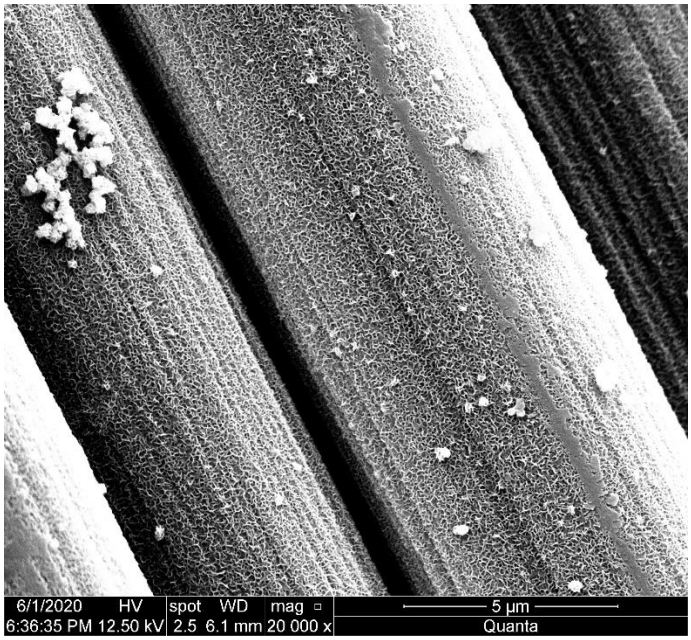

Figure 2.2 MOF Growth on Carbon Fiber

In comparison with ZnO, the benefit of MOF structures is its flexibility. The metal ion and linkers can be chosen to optimize a certain mechanical, electrical, or optical property [40]. Like ZnO, MOF can be used in a variety of applications. One application is in medicine, where Li et al.

used a zeolite imidazole framework for antibiotic extraction [41]. Another application is in superconductors. Yu et al. used various molecules for multi-component MOFs to produce superconductors with a high performance [42]. There are many other applications of MOFs such as sensors, fuel cells, and catalysts [43].

Much like with ZnO, there are various methods of MOF growth. Armstrong, Shan, and Mu compared two methods of growth, electrospinning and a solvent based chemical method [44]. With electrospinning, the MOF blended polymer solutions were passed through a needle under a direct current onto the surface of the fiber. While this method worked, there were issues of fiber breakup. They also used a secondary method of creating a growth solution for fibers to be soaked in. This method, when the fibers were soaked in methanol, resulted in uniform growth across the entire fiber mat. Lin et al. used only a chemical based growth methodology to grow the MOFs on the surface of the fiber [45]. Their method was similar to Armstrong's, clearing two growth solutions that were mixed together and the fiber mats were left to soak in that solution for 24 hours. Cleaning and drying the fibers finalized the growth process. Their growth method also showed uniform growth of MOF onto the fiber's surface.

Another method of growth is chemical vapor deposition. Li et al. grew cobalt based MOF onto a fiber's surface by combining electrodeposition and CVD [46]. First, cobalt was electro deposited onto the surface without spinning. Then the CVD process is used to convert the base cobalt into the MOFs. MOFs also increase mechanical performance of carbon fibers. Ayyagari et al. grew nickel based MOFs onto fibers using a hydrothermal method and found that the tensile strength of the fibers increased from 506 MPa to 560.6 MPa, along with a 40% increase in shear strength [47].

2.5 Methods for Measuring Interfacial Properties

There are many methods for measuring interfacial properties of composites, at various size levels [48]. At a nanoscale, nanoindentation is the main tool for mechanical testing as it has the

fidelity to perform in-situ tests on a single fiber level, along with being able to interact with the interface region. Nanoindentation works through an indenter tip that applies a force or displacement onto the testing surface. This load/force application results in a load-displacement curve, analogous to a stress-strain curve from typical material testing. From the unloading portion of the load-displacement curve, the hardness and reduced modulus of the sample can be found. The reduced modulus can then be further processed to get the young's modulus [49].

To get other interfacial properties, the load-displacement curve can be analyzed at various locations to compare maximum displacements, the maximum loads can be compared at various locations, or loads at which certain nonlinearities occur can be looked at. Gregory and Spearing used nanoindentation to perform modulus and hardness comparisons at various locations by varying loads and depths [50]. Wang et al. also used a nanoindenter to find interfacial shear and frictional stress [51]. This was achieved by indenting a fiber until it debonded, marked by a sharp change in the load-displacement curve. Essentially, the loading portion of the curve reached a certain displacement then a large jog to a much greater displacement marked the beginning of the unloading. Using that critical force at which the nonlinearity occurred, the shear strength was found to be 323 MPa and frictional strength was found to be 312 MPa for that composite.

Another nanoscale characterization technique is modulus mapping. There are two kinds of mapping possible with a nanoindenter. One is with a map of indentations. For example, the indenter can perform 100 indentations in a 10 x 10 grid, collecting each load-displacement curve. Then, a map can be created of the hardness and reduced modulus of each point, with smooth transitions to the next point. Enrique-Jiminez et al. used this technique to measure the effect of graphene particles on the surface of carbon fibers [52]. They used a 25 x 25 grid of indents to measure the hardness on the fiber's surface, interface, and matrix region, creating a map of those

values. These maps were compared for both bare fibers and modified fibers to find that the interface region had a slightly higher modulus than the bare fiber's interface. Randall et al. also used a similar procedure on naval brass to compare properties of each grain and on various secondary phases of the material [53].

The other form of modulus mapping is using a dynamic mechanical analysis (DMA) approach. In this case, the tip acts as a simple harmonic oscillator, taking the given load and frequency from the nanoindenter machine to collect the response amplitude and phase from the material. From there, classical DMA theory can be used to derive certain variables like storage modulus and loss modulus [54]. This test is done during a scan, be it atomic force microscopy (AFM) or scanning probe microscopy (SPM). As the tip rasters along the surface of the sample, the load amplitude and frequency are applied to get a data point at every raster pixel. This results in a map of the sample's surface that contains data of each variable. Asif et al. used this method to map a carbon fiber's surface to look at the change of storage modulus throughout the sample [55]. They also showed profiles of the storage modulus, showing exactly how the storage modulus changes throughout the x location on the image. Gu et al. took this one step further to analyze the change in moduli at the interface [56]. Using modulus mapping, they were able to plot the change in storage modulus along the x-axis of the sample. Analyzing the profiles, they were able to see how the modulus transitions from matrix to fiber, using that to approximate the size of the interface layer and average modulus at the interface. Using this, they found the interface of a T300 carbon fiber composite to be 118 nm and a T700 composite to be 163 nm.

Outside of the nanoscale, there are other interfacial characterization methods as well. One such example is a microbond test. The microbond test involves a single fiber being pulled out of a droplet of matrix. The important factor in this test is the force at which the fiber debonds, used to

find interfacial fracture properties. Nishikawa et al. used this method to quantify the interfacial shear strength of the fiber, which varied greatly from 64 to 108 MPa (average of 92.3 MPa) [57]. Another microscale test is a single fiber fragmentation test. This test is done with a single fiber encased in a dog bone structure of matrix. Then, the sample is pulled axially, until the fiber breaks. As the fiber fragments, the axial stress will become 0. The shear strength of the interface can then be found using the stress at which the fiber breaks, along with the length of the fiber at that time. Feih et al. developed a testing procedure for the fiber fragmentation test, with a carbon fiber composite [58]. They found that a resin and fiber sample had an interfacial shear strength of 18.5 MPa, but with a slightly modified fiber the interfacial strength increased to 53.8 MPa.

2.6 Nanoindentation Based Single Fiber Push-In Testing

In this study, nanoindentation will be used for single fiber push-in testing. Single fiber push in consists of the indentation tip pushing in the fiber from the top. This compression will result in debonding at the interface's critical stress. Debonding is characterized either by a large jog nonlinearity or by a change in linearity of the load-displacement slope. From these tests, usually a basic shear-lag model is used to find the equation for interfacial shear strength. Hinoki et al. used this method of testing for a SiC/SiC composite with varying thicknesses of fibers [59]. Their testing found that the load-displacement curve would have a big jump in data when debonding would occur and used this to find the interfacial shear strength. From their tests, they found that for thinner fibers of less than 1 micron, the interfacial shear strength was around 300 MPa. Rodríguez et al. performed a similar experiment on a carbon fiber/polymer matrix [60]. Their goal was to develop a method for finding interfacial shear strength on a fiber/matrix composite. They also had representative load-displacement curves for their push in tests, however their analysis was slightly different than Hinoki's. Their shear-lag model led to a different interfacial shear strength equation, using the slope of the linear loading curve. In Hinoki's paper, they used only the

debonding load and fiber geometry; Rodríguez added the slope as well. This is not a major issue as the slope term simply adds a scaling to the shear strength, but the difference in derivation is present between the two papers. Rohrmüller et al. used single fiber push-in testing for fiberglass composites [61]. Their interfacial shear strength equation was similar to Hinoki's. Through their experimentation, they found the interfacial shear strength for the fibers to be around 65 MPa. From this, the interfacial shear strength equation derived from Hinoki's analysis was used in the experimentation portion of this study, due to its widespread use in literature.

2.7 Modeling Approaches for Interfaces

Modeling can be used to generalize experimental findings. In order to understand how experimental results can be used in modeling, a brief survey is presented in this section in terms of both wetting and mechanical modeling can be used in conjunction with experimental results to explain interfacial modification.

Various methods exist for modeling interfacial interactions. Beginning with wetting, models can be made to analyze the behavior of the epoxy at the fiber's surface. Chen et al. used a COMSOL model to gain insight into the adhesion behavior of epoxy and fiber [62]. Their model used electrowetting to improve bonding, so the model featured fiber, air, and epoxy with the fiber having electrical properties to it. Their wetting model came from a combination of various models; Maxwell, Navier-Stokes, and Cahn-Hilliard models were all combined for this electrowetting analysis. Using their model, they found that the presence of electricity through this electrowetting procedure improves the wetting of the epoxy, as the electrical current attracts the epoxy down to the fiber. Another wetting model comes from Sathyanath and Kalpathy [63]. Their model predicts the wetting behavior of thin films on porous structures. This can be adapted to the carbon fiber case as well, simply by taking the porous structure as the carbon fiber's modified surface (or no pores for bare surface), and the thin film being the small layer of epoxy on top of the fiber. Their

model uses a modified Navier-Stokes equation to find the height of the thin film on top of the porous structure. While this model does not directly explain carbon fiber modification, it can be adapted to the problem. These various wetting models use parameters such as surface and interfacial tension, along with viscosity and other parameters. By tuning these parameters based on matrix type and nano-species type/geometry, ideal performance can be gained.

In terms of push-in modeling, a different approach is used. Typically, finite element modeling uses linear elastic behavior in its solutions. However, debonding results in fracture of the inner surface, which cannot be modeled by linear elasticity as debonding is a nonlinearity. Thus, a specific model is used known as a cohesive zone model (CZM). CZM models the fracture zone (debonding area) by having external work absorbed as fracture energy [64]. In the case of nanoindentation, this fracture zone is the interface. The interface layer would be modeled as a separate material, behaving with a traction-separation law. This traction-separation behavior is similar to stress-strain, with a damage initiation region and damage evolution region.

As the traction (stress) increases to its maximum, damage occurs. In the traction separation definition, the area under the curve is the fracture toughness, just as the area under a stress strain curve is the toughness of the material. The damage is then propagated through that element until the next element, and so on. Using CZM, a fracture zone can be modeled without fear of nonlinearity. Li et al. used a CZM to model nanoindentation [65]. This is done using geometry where the fiber is surrounded by a thin interface layer and then the matrix region. The fiber and matrix have their own definitions as elastic materials (Young's modulus, Poisson's ratio, etc.), however the interface follows the traction-separation rule. Using the definitions of the various CZM parameters, the model was generated and followed the experimental results well. Xu et al. used a similar CZM model to verify nanoindentation results [66]. While fiber and matrix had their

own isotropic material definitions, the cohesive zone interface was modeled using a bilinear traction separation law. Cohesive materials are defined using a traction vector, separation vector, and stiffness matrix. The damage portion of the definition has many options, but a usual choice is the quadratic stress definition. Finally, softening was defined using a linear function. Using this, the interfacial shear strength was used as the variables of the quadratic stress function, and fracture energy was used as the area under the curve. With that model and the experimentally gained variables, the experimental data was verified.

3 Experimental Approach

This section goes over the methodology concerning the creation of the as-is and modified carbon fibers, as well as other experimental samples. Procedures are outlined to create similar nanoindentation samples, as well as general testing procedures for the various characterizations. Finally, the methodology behind the computational modeling aspect of the research is discussed.

3.1 Materials

The carbon fibers used in this study were Thornell T650 polyacrylonitrile (PAN) based fibers in a plain weave, procured from Solvay, Inc. Individual tows of fibers were taken out of the weave to be used for nanoindentation and nano-species growth. The epoxy used was Aeropoxy, a medium viscosity, 2 part epoxy obtained from PTM&W Inc. The epoxy consists of PR2032 resin, and PH3665 hardener.

To synthesize the ZnO crystals, the following chemicals were obtained from Sigma Aldrich in laboratory grade: ethyl alcohol, hexamethylenetetramine (HMTA), nitric acid, sodium hydroxide, zinc acetate dihydrate, and zinc nitrate hexahydrate. Likewise, synthesizing MOF used the following lab grade chemicals from Sigma Aldrich: methanol, 2-methylimidazole, and nickel nitrate hexahydrate.

Other materials were used to assist in the various experimentation processes. Creating the nanoindentation sample made use of the chemical FibRelease, as well as sealant tape. Various forms of double sided tape were used to attach samples to grinding and polishing stubs, nanoindenter base plates, and SEM stubs.

3.2 Equipment

Various equipment assisted in multiple steps of this research. To cure the fiber and epoxy samples, a Yamato DX402C oven, shown in Figure 3.1, was used. For grinding and polishing, a

Buehler MetaServ 250 was used, shown in Figure 3.2. To assist, 600 and 1200 grit sandpaper was used, as well as alumina suspensions in 5 and 3 μm sizes with a polishing pad shown in Figure 3.3.

Figure 3.1 Drying Oven for Composite Samples

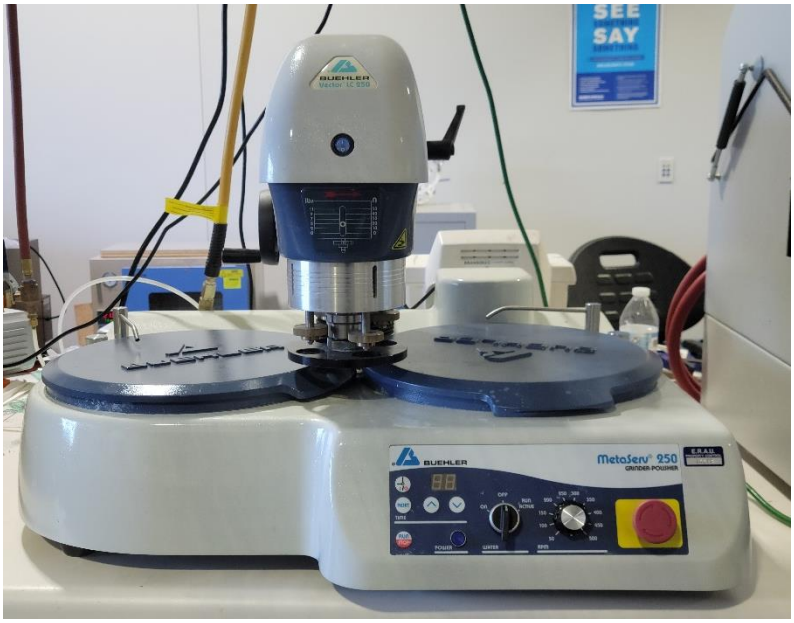

Figure 3.2 Grinder-Polisher Machine

For the desizing of carbon fibers, an MTI OTF-1200X tube furnace was used. To cut the composite samples, an OMAX Maxiem 1515 waterjet cutter was used.

Figure 3.3 Grinding and Polishing Pads, and Alumina Polishing Suspensions

For microstructural analysis, a FEI Quanta 650 SEM was used, shown in Figure 3.4, along with a Cressington 108 sputter coater for gold coating. Finally, the majority of testing occurred using a Bruker Hysitron TI-980 TriboIndenter, shown in Figure 3.5.

Figure 3.4 FEI Quanta 650 SEM

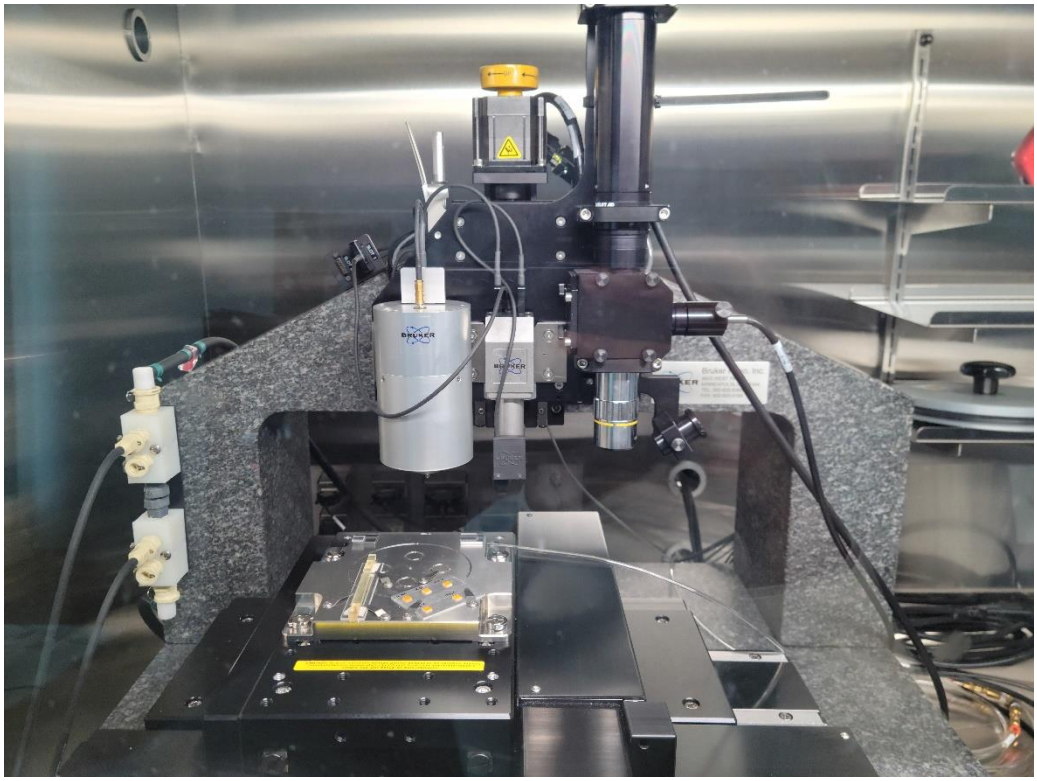

Figure 3.5 TI-980 NanoIndenter

3.3 Nano-Species Growth Procedures

The growth procedure started with the base fiber tows. The first step was to get rid of the sizing, known as de-sizing. The sizing material is a polymeric coating on the fibers bonded during production to help protect the individual fibers from the elements and from fraying. In order to remove the sizing, the fiber tows were put in a tube furnace, with a nitrogen atmosphere flowing through the tube. The furnace was heated to 550 °C, and the fibers were allowed to heat at that temperature for 1 hour. The tube furnace setup is shown in Figure 3.6. The fibers were then cooled to room temperature outside the oven. Some desized tows are also taken as reference fibers, called "As-Is" in further experimental results. The rest of the tows were used in the nano-species growth process.

Figure 3.6 Fiber Desizing Tube Furnace

One more common step was performed for both nano-species growth, called acid activation. This step slightly etches the fiber surface, creating acidic groups on the surface to promote the bonding of the nano-species. To do this, a solution of nitric acid diluted in deionized (DI) water was stirred together until mixed well. Then, the solution was placed in a glass container and fibers were submerged into the solution for 24 hours. Afterwards, the fibers were rinsed with water to remove the surface solution and allowed to dry in an oven to further remove excess liquids.

3.3.1 ZnO Growth Procedure

The first step in the ZnO procedure was the seeding stage, which required a mixture of 100 mg zinc acetate dihydrate, 40 mg sodium hydroxide, and 400 ml ethyl alcohol. This mixture was stirred at 400 rpm for 1 hour. Then the acid activated fibers were dipped in the solution for 2 minutes and dried in an oven at 150 °C for 15 minutes. This dipping and drying procedure was repeated 5 times for effective coverage of the solution. The next phase was the growth phase. This uses 2 solutions – the first used 13.98 g zinc nitrate hexahydrate and 1800 ml DI water stirred for 40 minutes using an ultrasonic processor; the second used 6.3 g of HMTA with 1800 ml DI water mixed for 40

minutes. The two solutions were then mixed together using an ultrasonic tip-sonicator for minutes. Then, the mixed solution was poured into glass containers so the fibers can soak in the solution. The seeded carbon fibers were soaked into 600 ml batches of the growth solution for 6 hours at 93 ℃, covering the container with foil to reduce evaporation. After the growth process, the fibers were left to dry in the oven at 150 ℃ to remove excess moisture. This growth procedure was adapted from Kumar et al. [31].

3.3.2 MOF Growth Procedure

As a disclaimer, this procedure was developed by Dr. Marwan Al-Haik and processed by Derek. Derek prepared the samples for use in this research; however, the process outlined below is the general growth process for MOF.

The MOF growth procedure required a growth stage. The growth solution required a source of metal ions and a secondary solution. The metal ion solution was a 0.65 M nickel nitrate hexahydrate and methanol solution, and the secondary solution was a 0.14 M 2-methylimidazole in methanol. The 2 solutions were stirred at 400rpm for 6 hours, then mixed together and stirred again for 10 minutes. This mixed solution was put in a glass container, and acid activated fibers were submerged in the solution for 24 hours. After, the fibers were repeatedly washed with ethanol and dried in an oven for 24 hours to remove all moisture, at 93 ℃. The MOF growth procedure was adapted from Ayyagari [47].

3.4 Microstructural Characterization

Once the three fiber tows (As-Is, ZnO, MOF) are ready, they can be imaged in the SEM for geometrical characterization. Using an SEM stub, a piece of carbon double-sided tape was put on top. Then, one tow of fiber was put on the tape, and the ends were taped with copper tape. Then, the fibers were coated with gold for 40 seconds at 35 mA to ensure a strong coating. Then, the stub was placed in the SEM for analysis. The As-Is fiber diameter was measured as a reference, and

the modified fibers were measured for both diameter and nano-species dimensions. These images and measurements are shown in Section 4.1.

3.5 Composite Sample Preparation

The three fiber tows were also used in creating the composite sample for nanoindentation. To do this, an aluminum plate was used as a base, with 4 pieces of sealant tape creating a moat, with the inside area measuring about 7.62 cm x 7.62 cm (3 in x 3 in). A thin layer of FibRelease was coated in the middle of moat so that the composite does not adhere to the plate. Then, the separate fiber tows were placed along the length of the moat, pulling them taut. Then, one more layer of sealant tape was put on top of the first, sandwiching the fiber between the two layers of tape. Some tape was also used on the outside to keep tension in the fibers. Inside the moat the Aeropoxy was poured in. Aeropoxy was mixed using a 100:27 weight ratio of resin and hardener, and approximately 50 ml of epoxy was used to fill in the moat. An image of the composite curing setup is shown in Figure 3.7. After checking for leaks in the moat, the plate was put in the oven for 2 hours at 93 °C.

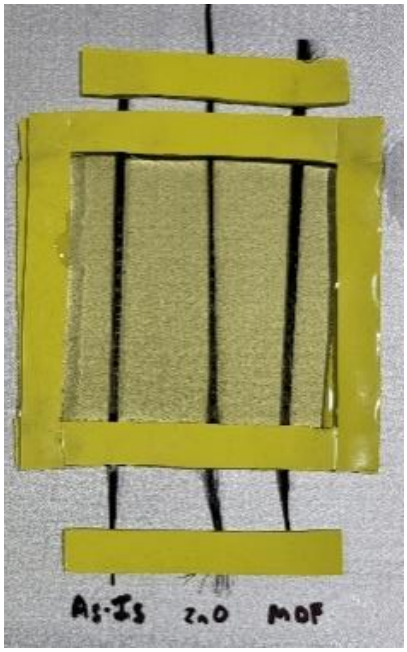

Figure 3.7 Composite Curing Moat with Fibers Inside

Once cured, the composite was pried off the work plate and cut with the water jet cutter. This resulted in sized and straight-cut samples to work with. The sample was cut into 1 cm tall samples. Then, one surface of each sample was ground using both 600 and 1200 grit silicon carbide sandpaper and flowing water, using the Buehler rotary grinder-polisher machine. After grinding, the top surface was checked with an optical microscope to see how effective each sanding step was. Then, the surface was polished using the alumina suspension. Two alumina suspensions were used on a wet polishing pad: first 5 μm, then 3 μm. After each polishing step, the surface was checked under an optical microscope to ensure the effectiveness of the polish in removing the scratches. Then, the sample was cleaned using a sonicator in DI water for 10 minutes, then dried. Figure 3.8 shows the initial cut sample (left), and the sample after polishing (right). The samples were then taped on a thin aluminum plate with a hole cut into it. This hole exists such that the fibers are not being supported by the plate, so that they are allowed to slide vertically if debonded.

Figure 3.8 Initially cut sample (left), and sample after grinding and polishing (right)

3.6 Nanoindentation

The sample was then placed onto the nanoindenter base plate using the built in clamps. The nanoindenter is an optical-driven system, with an optical microscope being used to look around

the sample and choose testing areas. The first step in using the nanoindenter is to find the sample surface and create a sample zone such that the system knows where the user wants to test. This is done by moving the stage and using optics to see the surface. Figure 3.9 shows the surface of the composite sample under the optics. Looking at the optics, there are some small scratches around the material, but mostly the sample surface is clean. The circular shaped objects are the fibers, with some of them being white and black. The black fibers are not as polished as the white fibers, as the white fibers are completely polished carbon fibers that appear white as the polish appears to make the surface of the fiber reflective.

After setting up a sample zone for each type of fiber, the next step was to perform calibrations. These calibrations, such as the tip to optics or the air indent, ensure that the system and machinery are behaving as they are specified. The air indent tests that the plates inside the force transducer can actuate completely and apply their load, and tip to optics ensures that the tip goes exactly where the microscope specifies it to go. The last calibration to do is a tip-area function. Nanoindentation is heavily dependent on contact depth and contact surface area, so the tip-area function essentially makes the system create the tip using a 5^{th} order fitting function. This would make sure that the system knows the exact contact depth on every indent and the exact surface area of the tip at every depth.

The nanoindenter is a system that has many possible functions; some of these functions are a high load indent, low load indent, nanoDMA, xSol temperature based indent, nano scratch, and nanoECR electrical based indent. In this research, testing was done using a low load indent, high load indent, low load xSol, and low load modulus mapping (a derivative of nanoDMA). The following sections will introduce each testing module, giving an overview of how each works and the settings used in this research.

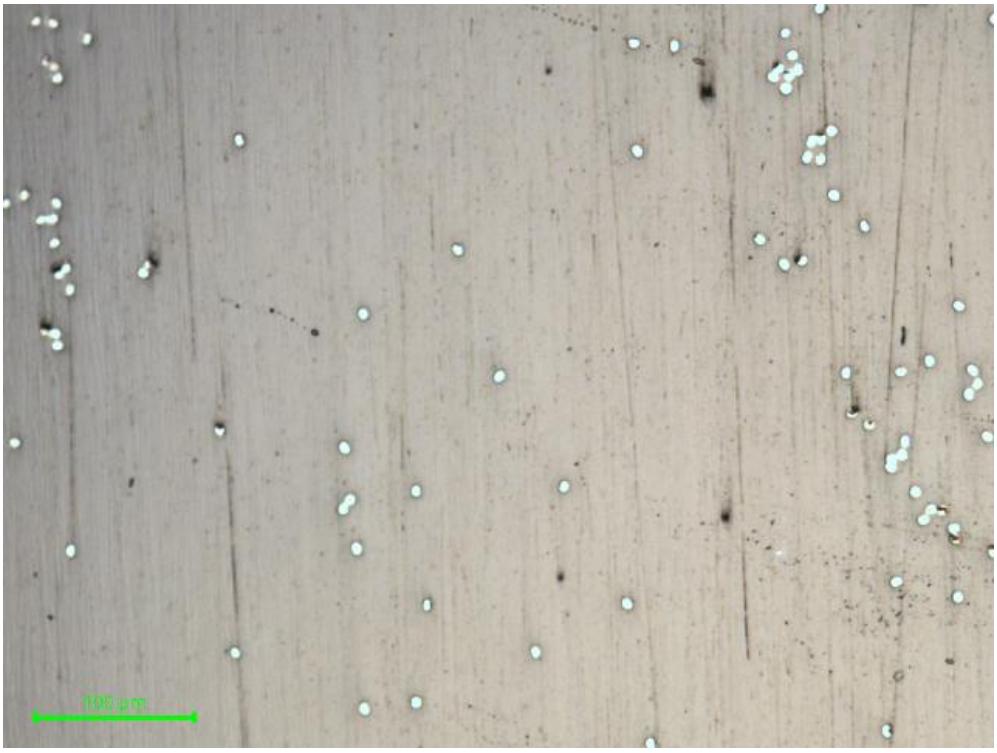

Figure 3.9 Sample Surface Under Optics

3.6.1 Low Load Scanning

Low load scanning is a function that allows for the imaging of the indentation surface at a nanometer level. It is a form of scanning probe microscope (SPM), wherein the tip rests on the indentation surface. Then, with a set force, the tip of the indenter performs a raster scan of the surface, using the force reaction to draw a force gradient scan, as well as a topology graph. This allows for the imaging of the fiber's surface to see indents on the surface and behavior of surrounding geometry. Along with that, some basic analysis can be done such as surface roughness calculations. In this work, the SPM scanning was used to image the surface of the fiber and nearby epoxy to both get surface roughness and to confirm indentation on the fiber. For high load indentation, the SPM scanning is especially helpful in correlating specific nonlinearities. In this work, typical scan sizes were 40 x 40 μm at 5 μN, with a 1 hz scan rate.

3.6.2 Modulus Mapping

Modulus mapping is a function of the nanoDMA, combining SPM scanning with the DMA function. Modulus mapping requires a setpoint fixed force along with a dynamic force amplitude and frequency. The nanoDMA system can be modeled by a single degree of freedom damped harmonic oscillator, which uses the input signal and output response to find the amplitude and phase of the response. These two values can then be used to find stiffness and damping, which can then be used to find storage and loss modulus. In this way, the modulus mapping can create a map of variables such as phase or loss modulus. Essentially, each pixel of the SPM scan will be a data point of some variable of interest. Modulus mapping is used to analyze the interface of the fibers by seeing the variation of loss and storage modulus throughout a profile of epoxy and fiber. In this research, the setpoint force of the mapping was 5 μN with a dynamic load of 2 μN and 200 hz frequency. The scanning rate was 0.1 hz with a scan size of 40 x 40 μm and 512x512 resolution.

3.6.3 Low Load Indentation

Low load indentation makes use of the low load force transducer in order to perform a simple indentation on the top surface of the fiber. It performs an indent using a certain load function, constantly measuring displacement of the tip to get a load-displacement curve. Using the unloading curve of the indenter, the nanoindenter program can find the hardness and reduced modulus of the sample. The area between the loading and unloading curve can also be integrated, which gives a measure of the toughness of the sample. In this work, 3 indents were performed on each fiber to get an average load-displacement plot for comparing maximum displacement. Epoxy indents are also used as a baseline comparison to all fibers. These indents followed a 5 second loading phase until maximum load of 10 mN, 2 second hold phase, and 5 second unloading phase. The area between curves was also calculated and compared. Indents were also performed at an elevated temperature of 71.1 °C to analyze the effect of heating on the load-displacement plots.

3.6.4 High Load Indentation

High load indentations mirror the low load indentation process, just with significantly higher forces. The benefit of high load is that it can apply a force such that debonding can happen. In this work, an 80 mN force was applied in a triangular load function at 1 mN/s loading rate. Before the indent, there was a small pre-lift in order to remove the effects of creep. 3 fibers were indented, and the debonding force is found by averaging the three curves' debonding forces. SPM scanning supported the indents by scanning the fiber for indentation confirmation, as well as corroborating certain changes in geometry.

4 Results and Discussion

The first set of results shown are the SEM images with corresponding geometry measurements. Then, the nanoindenter results are shown, starting with the low load indentations. The high load results are shown next with the analysis to get the interfacial shear strength, followed by modulus mapping results. After that, the conceptual wetting considerations are explained, followed by a general discussion on all the results.

4.1 Microstructural Analysis

Microstructural analysis begins with the As-Is fibers. Figure 4.1 shows a bare carbon fiber with Figure 4.2 showing a measured fiber. The measurement of the fiber shows a diameter of about 7 μm. This is in line with the manufacturer specification of 6.8 μm [67].

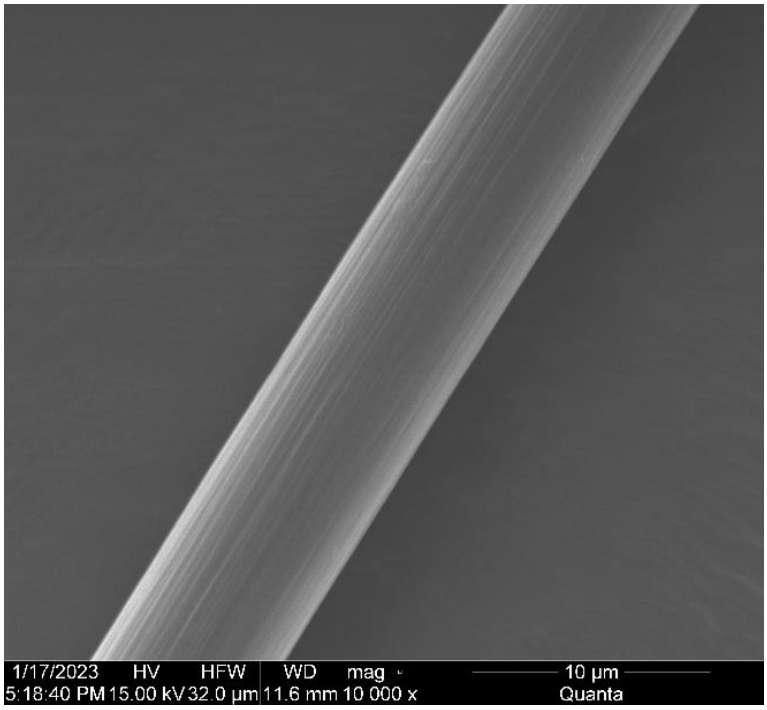

Figure 4.1 As-Is Fiber

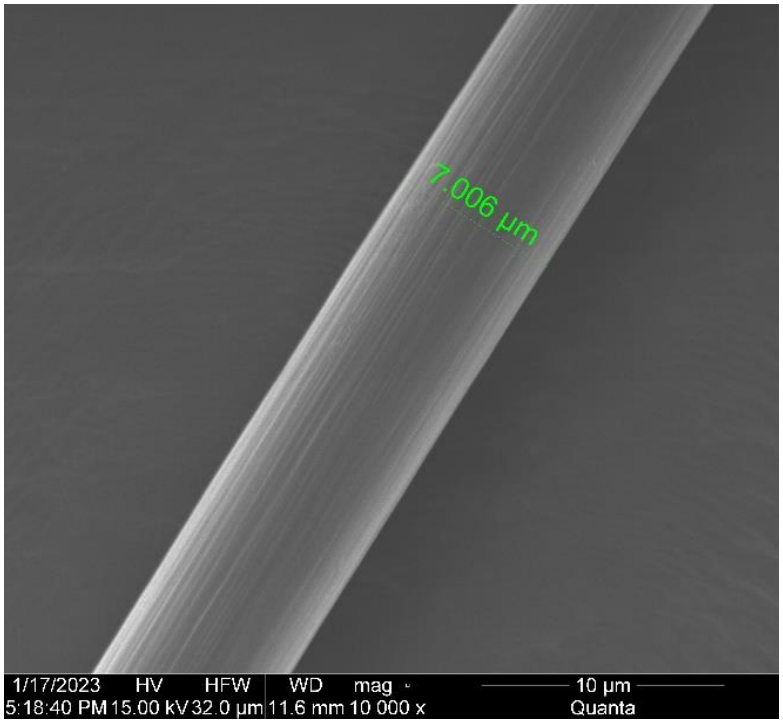

Figure 4.2 As-Is Fiber with Diameter Measured

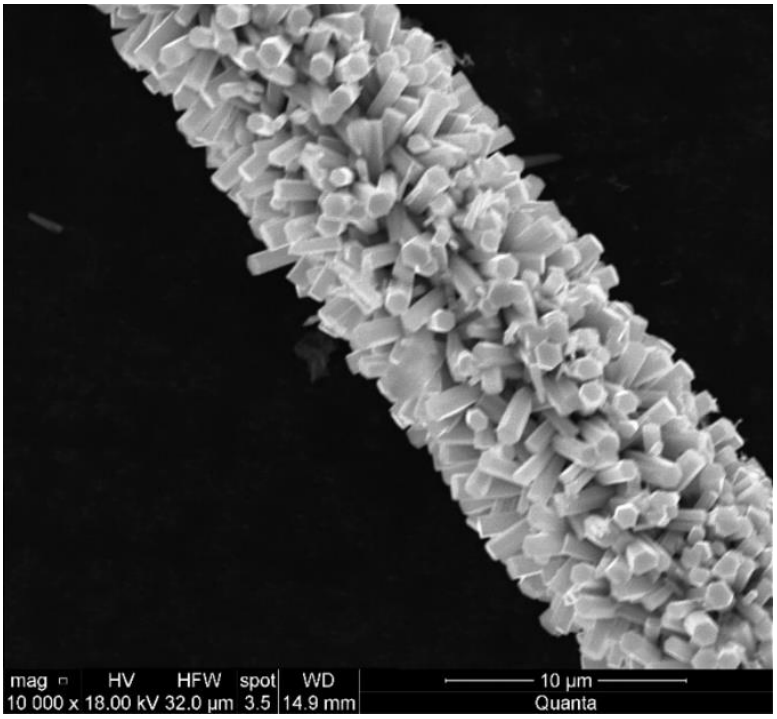

Figure 4.3 ZnO Growth on Single Fiber

Figure 4.3 shows a single fiber with ZnO growth. As seen by the image, the ZnO crystals can be seen grown radially and uniformly on the surface of the fiber, with the ZnO taking the expected shape of hexagonal prism. Figure 4.4 is a measured micrograph showing the diameter of a set of crystals. The diameters seem to center around 850 nm, with some crystals being smaller around 700 nm and others being larger around 1000 nm. Despite this spread, generally most of the fibers average around 850 nm in diameter.

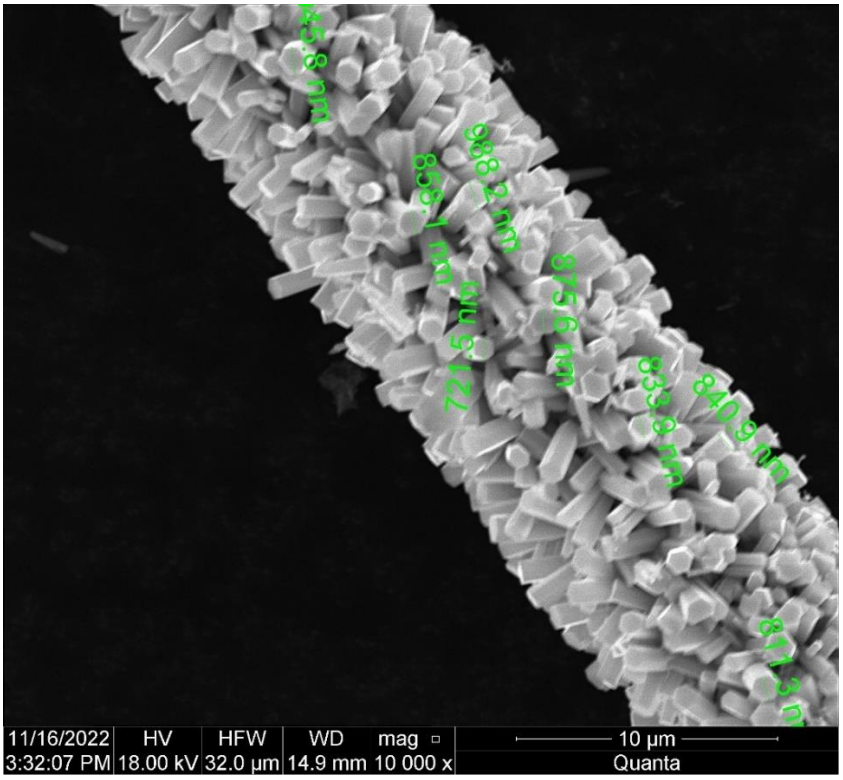

Figure 4.4 ZnO Fiber with Measured Diameters

Figure 4.5 shows the measured width of the ZnO carbon fiber. Since the growth is uniform on a circular surface, the height of the ZnO crystals would just be the new width subtracted by the original width, divided by 2. The ZnO modified fiber has its diameter extended to about 11 µm, so subtracting out the original 7 µm diameter leads to a difference of 4 µm. This means that the ZnO crystal height is approximately 2 µm.

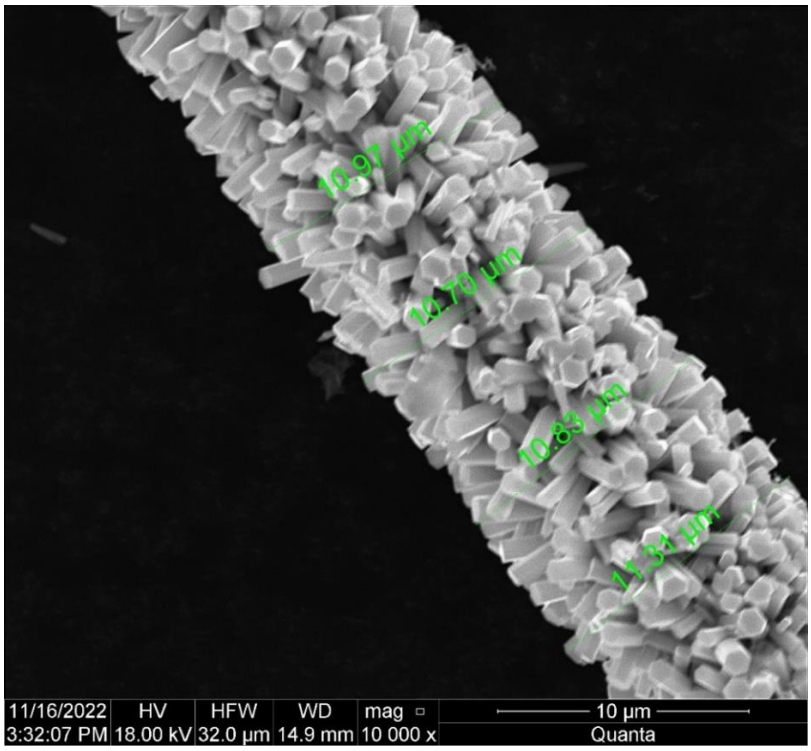

Figure 4.5 ZnO Fiber with Measured Height

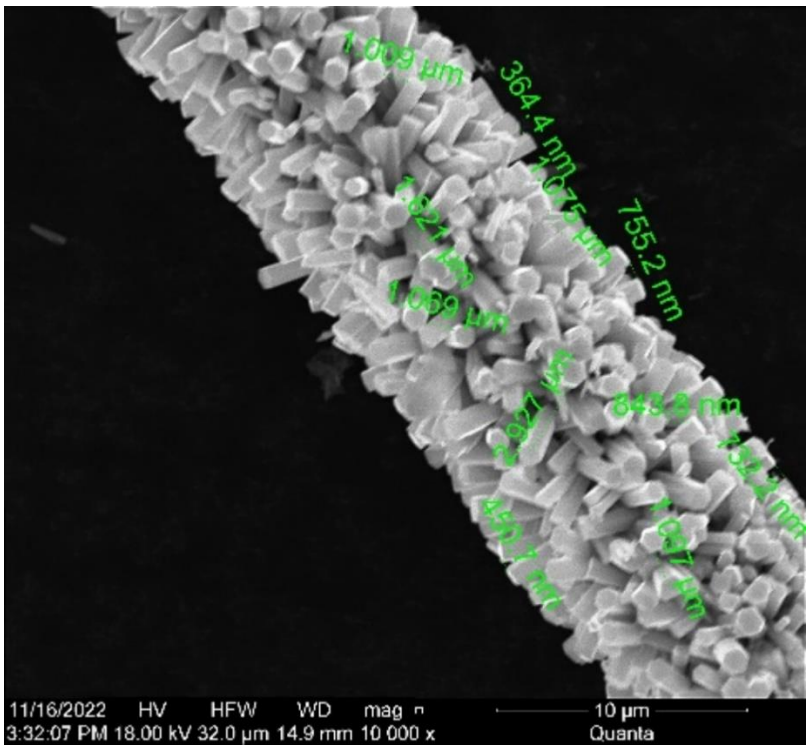

Figure 4.6 ZnO Fiber with Measured Crystal Spacing

Figure 4.6 shows the spacing between the crystals. This measurement varies as there are certain crystals that seem essentially connected to each other, and some that are as far apart as 3 μm. Overall, the ZnO micrographs show a uniform growth of ZnO crystals grown radially on the surface of the fibers, that are approximately 850 nm wide and 2 μm tall, which are spaced in varying amounts and orientations.

Figure 4.7 is a micrograph of the MOF growth on the T650 carbon fiber, sourced from Ayyagari [47]. Similar to the ZnO growth, MOF is seen to grow radially on the fiber in a uniform manner. The MOF takes the form of a porous, sponge-like crystalline structure. In this analysis, the flower structures will not be analyzed as they are not directly part of the fiber surface modification. The next set of figures shows the various measurements of the MOF structure. Figure 4.8 shows the diameter of the modified fibers, which is about 7.75 μm. This would indicate that the MOF height is about 375 nm.

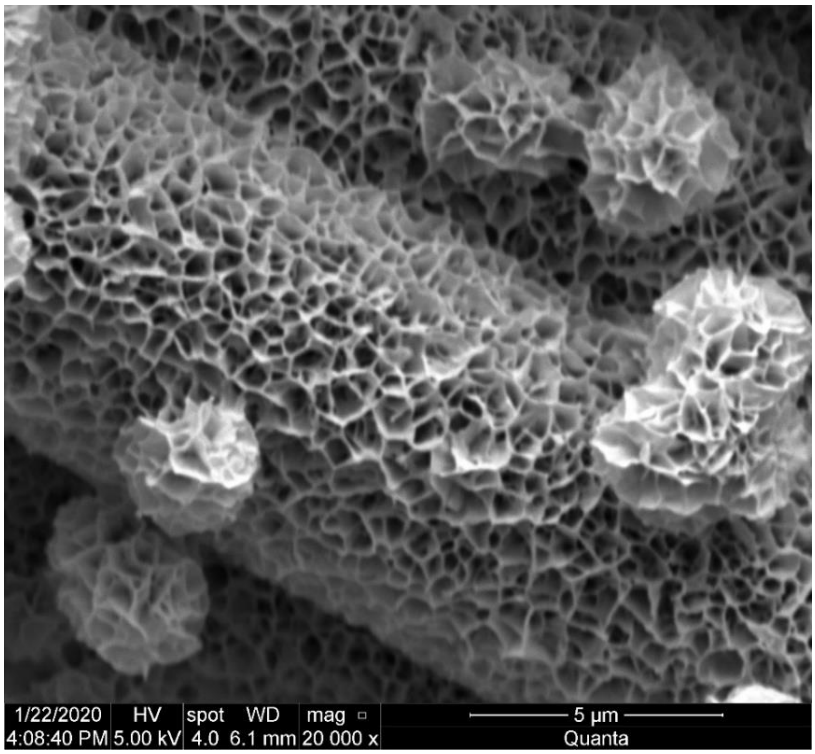

Figure 4.7 MOF Growth on Carbon Fibers [47]

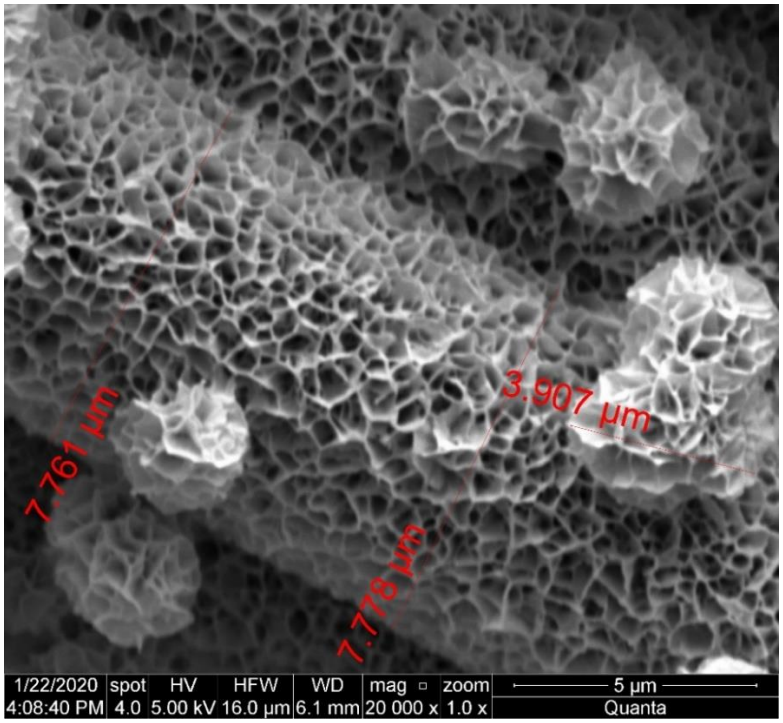

Figure 4.8 MOF Fiber with Measured Diameters

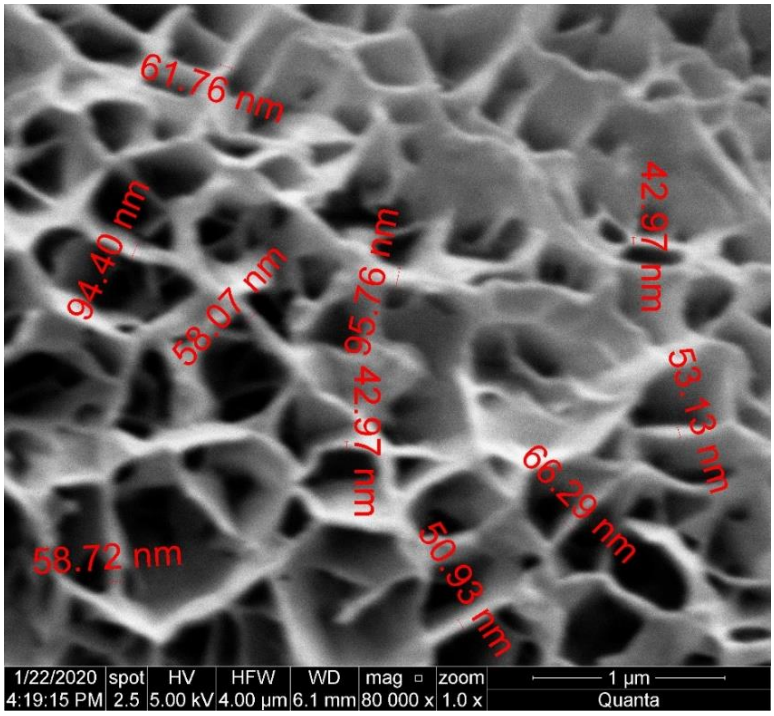

Figure 4.9 MOF Fiber with Measured Wall Width

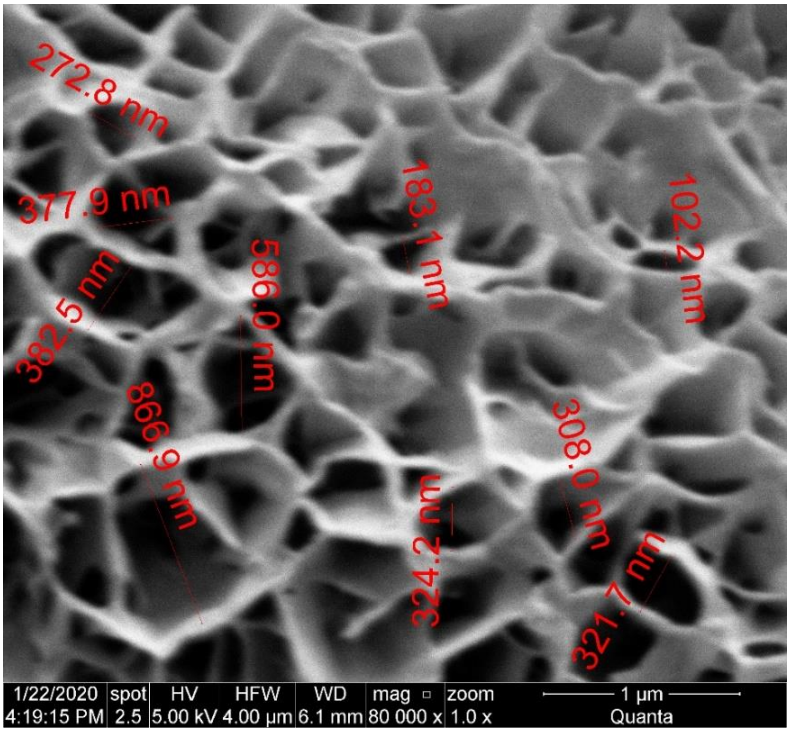

Figure 4.10 MOF Fiber with Measured Pore Width

Figure 4.9 shows the measurements of the MOF walls. These measurements are variable between 40 and 100 nm, though it is more likely the widths are around 60 nm. Figure 4.10 shows the width of the pores of the MOF. Again, it is variable, going from as little as 100 nm up to 900 nm. The micrographs indicate that the pore widths are likely to be on the smaller size, around 400 nm.

From the micrographs, the differences between the nano-species are clear. ZnO nanorods take on the form of large hexagonal prism ceramic structures, while MOF looks like a sponge shaped crystal structure. MOF is smaller than ZnO, but the smaller size of MOF would indicate that the surface area increase of the MOF would be greater than with ZnO. By taking the shape of the ZnO nanorods as hexagonal prisms and using micrographs, the ZnO nanorods increase the surface area of the fiber by 450 – 500%. On the other side, the MOF structure is also assumed to be loosely

based on a hexagonal prism. The range of geometry measurements is greater for the MOF; however, the measurements of MOF tend to be on the smaller end. Given this, the surface area of the carbon fibers is increased by around 1000%.

4.2 Nanoindentation

The various data sets from the nanoindenter are broken down into headings based on their function. To check polishing level, an SPM scan was taken of fiber and epoxy region and processed in the nanoindenter image processing application. From this, the surface roughness of the sample was shown to vary from 5 to 25 nm. Fibers were also found to not be flush with the surface, raising up around 300 nm from the surface.

4.2.1 Low Load Indentation

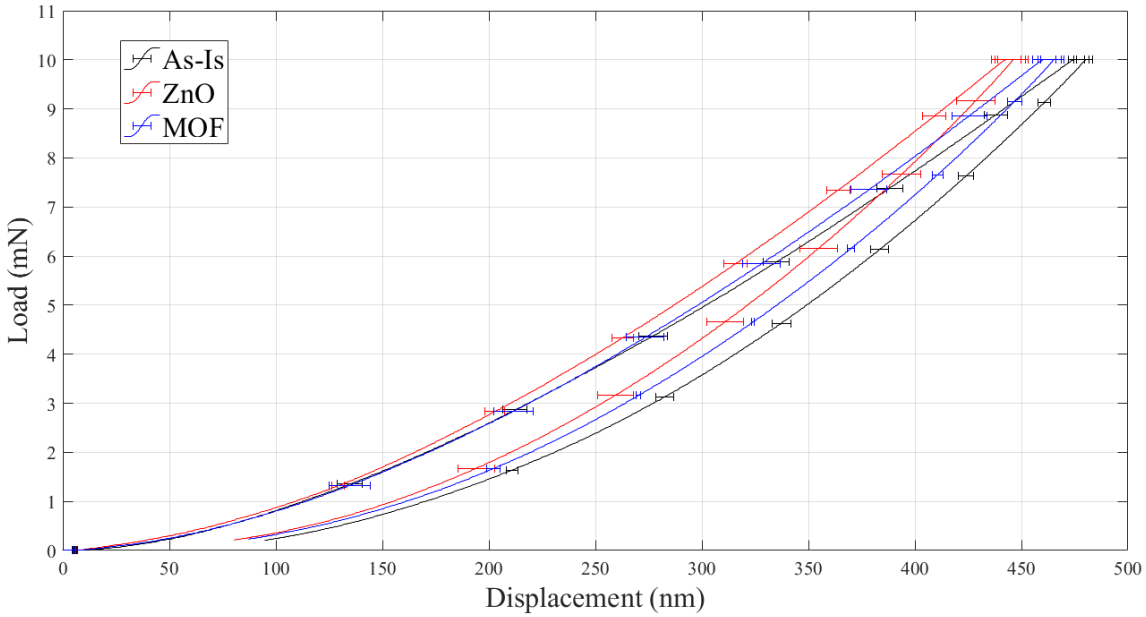

Figure 4.11 Comparison Load-Displacement Curves from Low Load Indentation

Figure 4.11 shows the average load-displacement curves for each of the fibers with error bars. These error bars come from the standard error of the data, out of 3 sets of data. Figure 4.12Figure

4.13, and Figure 4.14 show the constitutive 3 curves for each fiber, and Figure 4.15 shows the load-displacement curves for the epoxy.

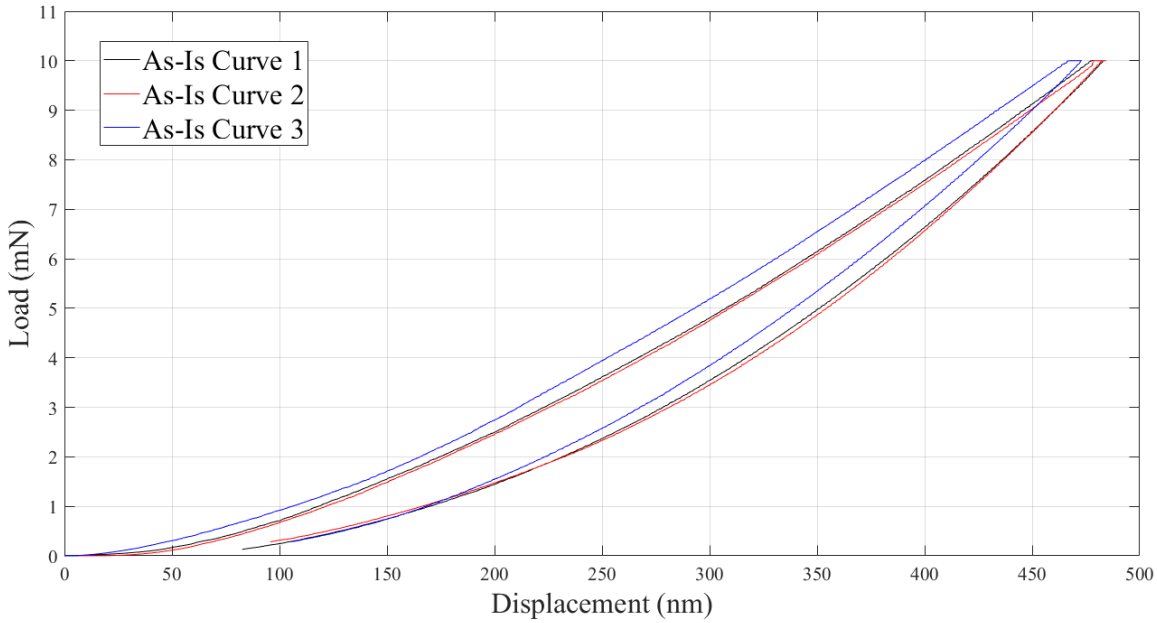

Figure 4.12 As-Is Representative Curves

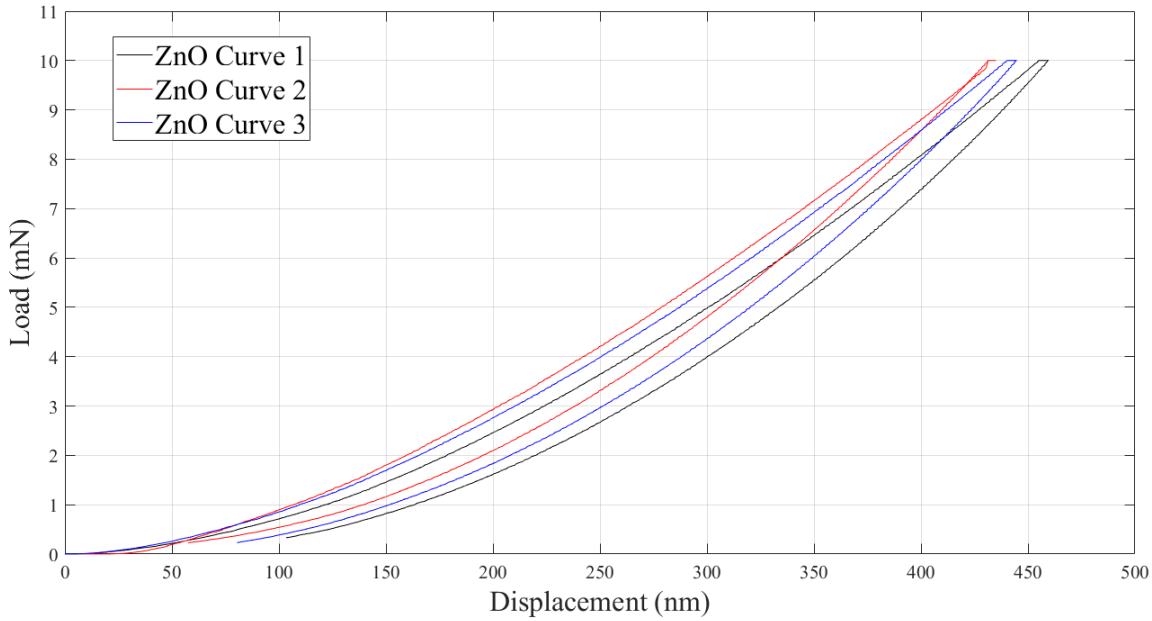

Figure 4.13 ZnO Representative Curves

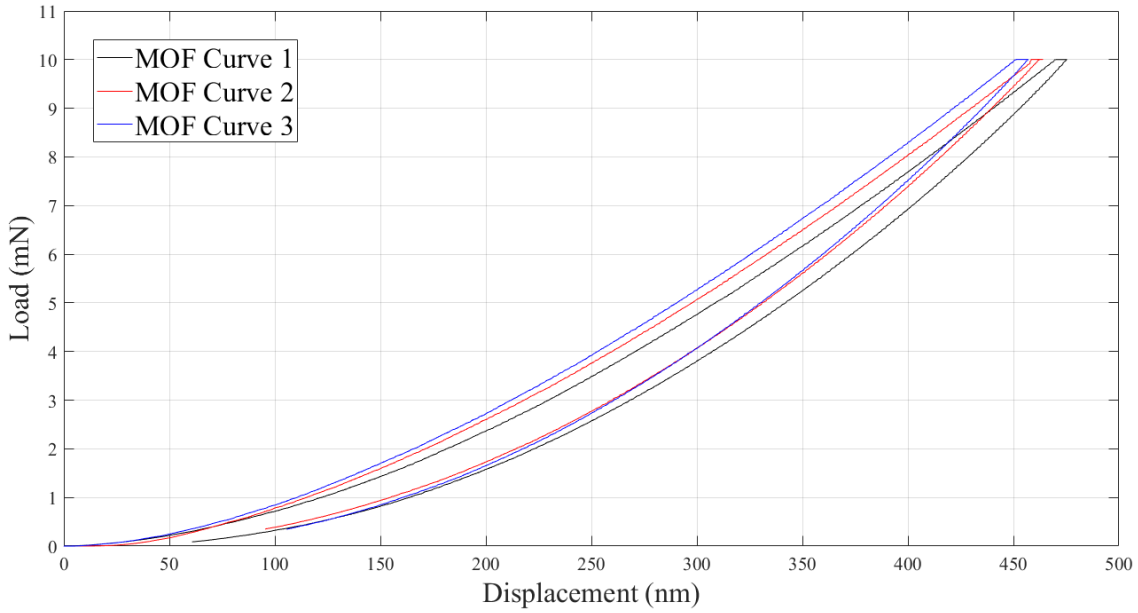

Figure 4.14 MOF Representative Curves

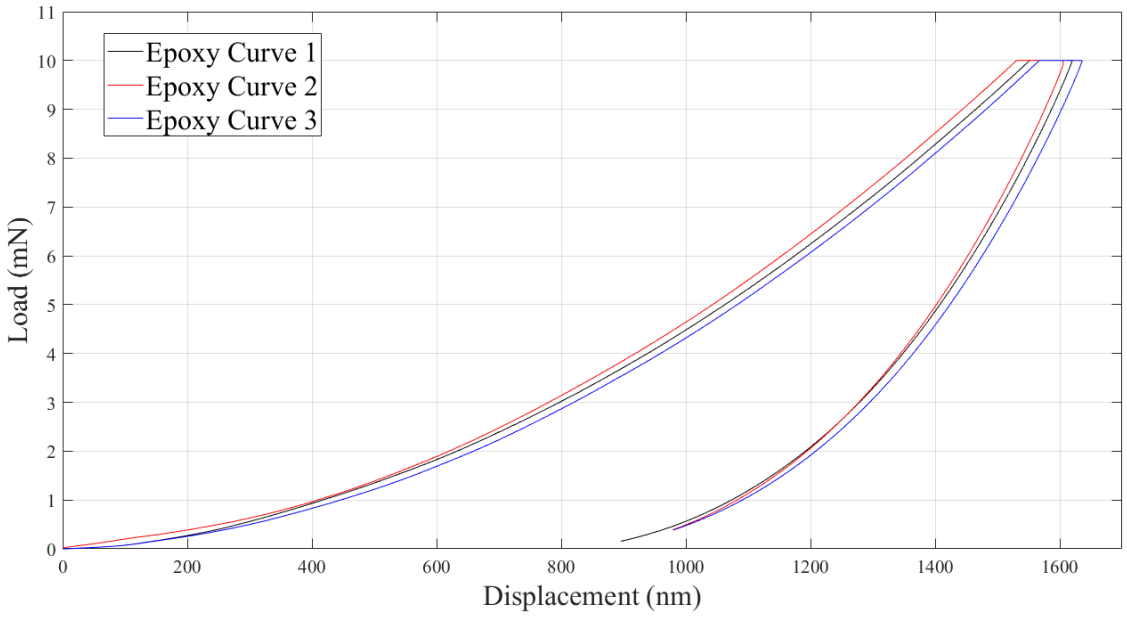

Figure 4.15 Epoxy Representative Curves

Figure 4.15 shows the epoxy representative curve, where it is clear the displacement in the epoxy is much greater than with the fibers. This is due to the epoxy being softer than fiber.

Additionally, the larger residual displacement of 1000 nm indicates a higher plastic response with epoxy. Figure 4.11 is a comparison of the average load-displacement curves of the three fibers. From this, it is clear that that the As-Is fiber has the greatest maximum displacement, followed by the MOF fiber then the ZnO fiber. The residual displacement is approximately the same for each, around 100 nm. One more variable of interest is the area between the loading and unloading curves. This integral would give a value that is indicative of toughness, though it is not the toughness variable itself. Visually, it is clear that the epoxy would have the highest area between the curves, followed by the fibers. However, the fibers look like they would all have similar areas. These areas along with the maximum displacements and residual displacements are given in Table 4.1 for each fiber.

Table 4.1 Comparison of Indentation Data at Room Temperature

	Maximum Displacement (nm)	**Residual Displacement (nm)**	**Area Between Curve (nm*mN)**
As-Is Fiber	480.1 ± 3.5	94.5	3406
ZnO Fiber	446.2 ± 3.4	80.4	3146
MOF Fiber	465.1 ± 3.7	87.2	3283
Aeropoxy	1619 ± 3.7	951.	6969

As expected, epoxy has the greatest displacement and area between curves. The fibers all have similar areas, and the As-Is exhibits the greatest maximum displacement of the three fibers. The next set of figures shows the SPM scans of each indent.

Looking at Figure 4.16, the indents on the epoxy and fibers are clear. There is minimal differentiation between each indent on the fiber, a product of low residual displacements. Summing up the low load data, there is no debonding occurring with the low load indents. There may be minimal local sliding occurring where the fiber and epoxy meet, but overall, the low load does not give information about debonding.

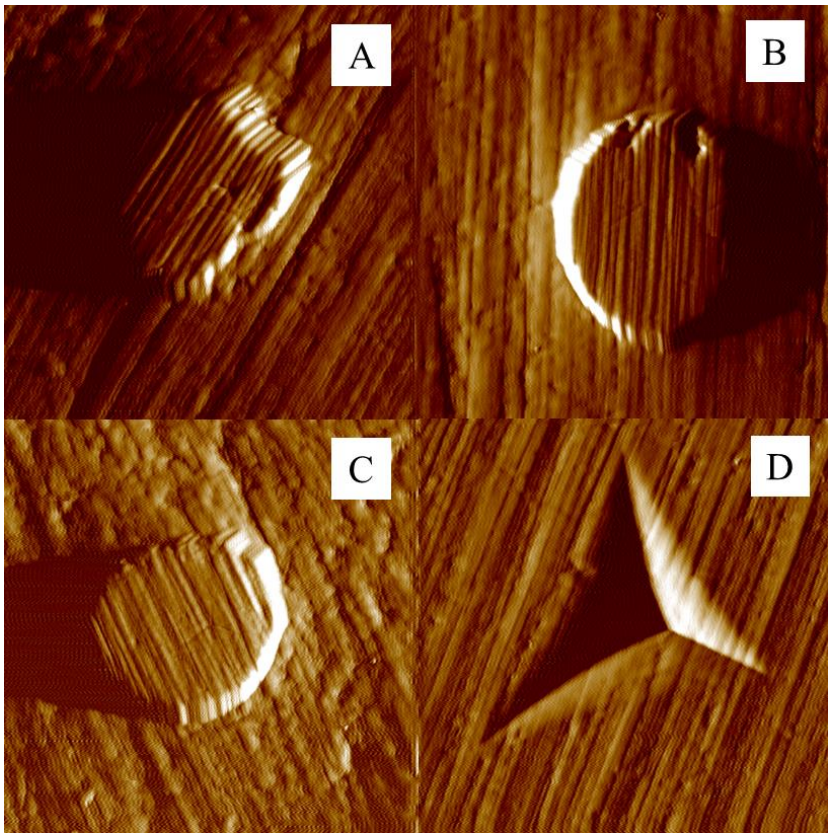

Figure 4.16 SPM Scans on (a) As-Is, (b) ZnO, (c) MOF, and (d) Epoxy

4.2.2 Low Load xSol

The next set of data comes with the xSol system data. These indents are using the same load function as the low load, just at the elevated temperature of 71.1 °C. Figure 4.17, Figure 4.18, Figure 4.19, and Figure 4.20 show the comparison curves between the average curves for each fiber and epoxy and the xSol results. The fiber indents are largely similar in behavior but have slightly higher maximum displacements and larger areas under the curve, but residual displacement is similar. The epoxy exhibits the largest change in behavior after heating, which makes sense as it is a thermoset. With heat, the material will soften slightly, allowing for higher displacement response.

Table 4.2 tabulates the three variables of interest for the xSol data.

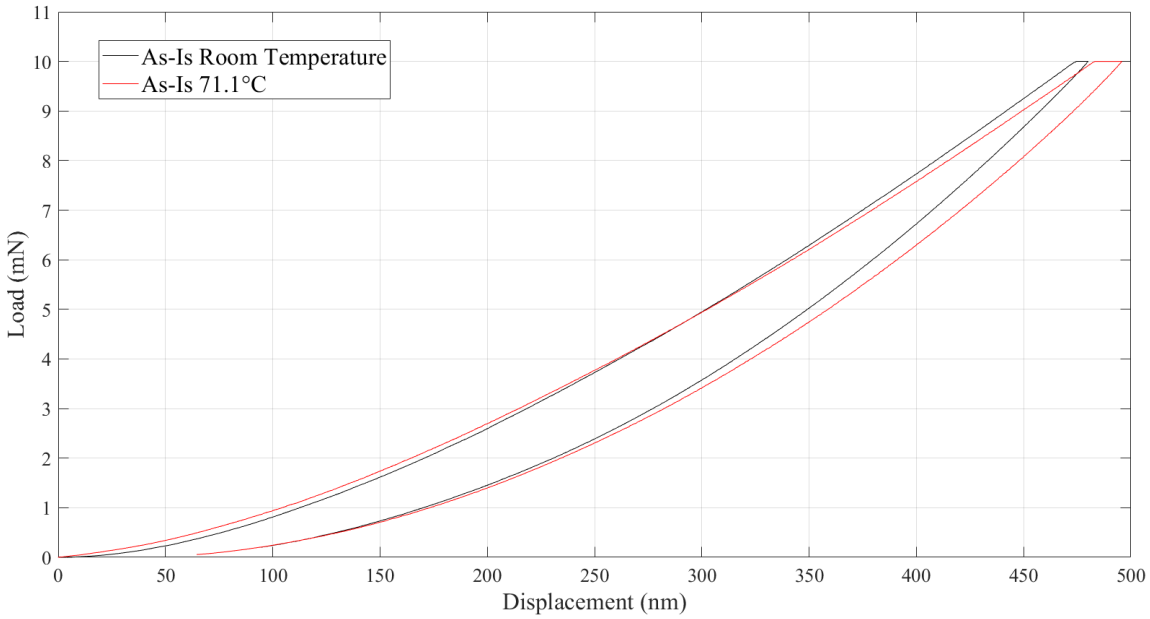

Figure 4.17 As-Is xSol Comparison

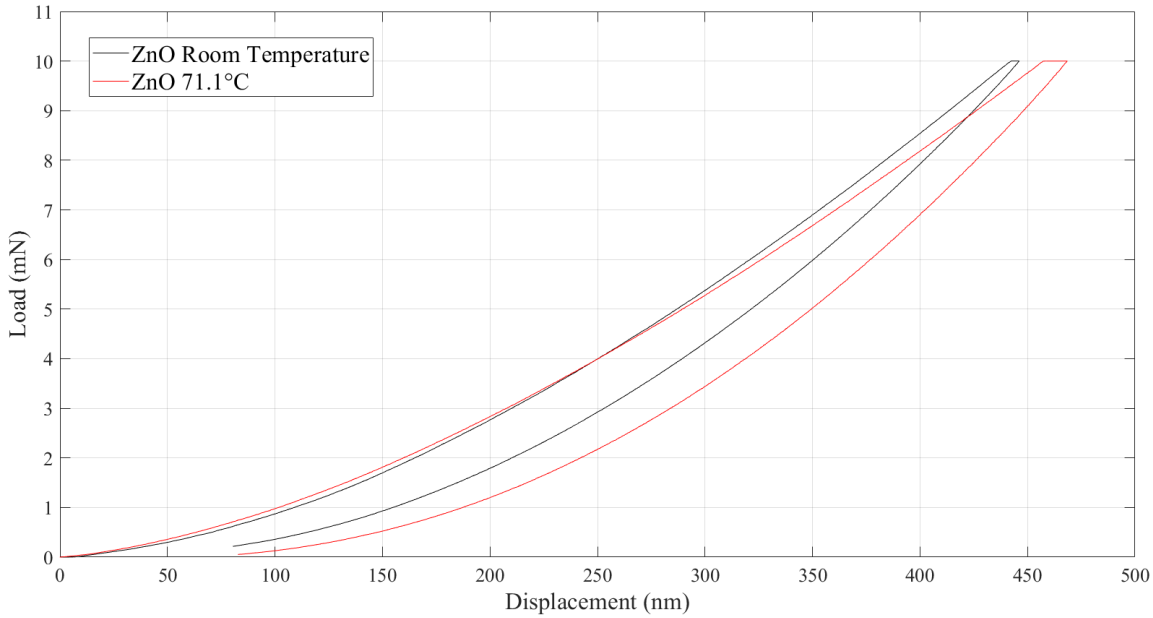

Figure 4.18 ZnO xSol Comparison

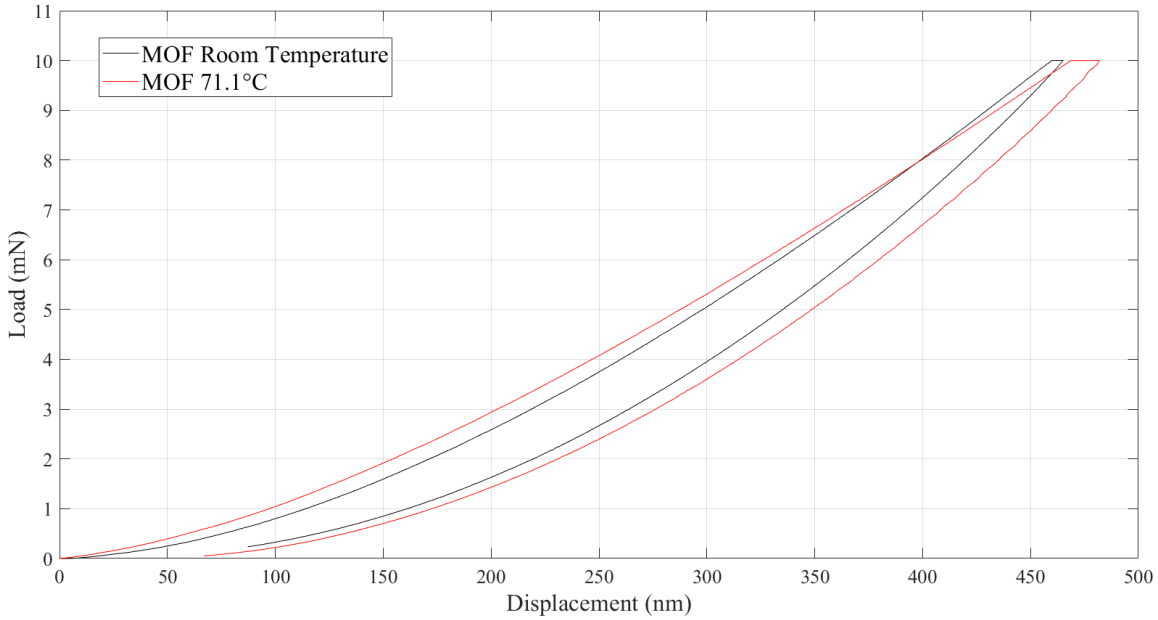

Figure 4.19 MOF xSol Comparison

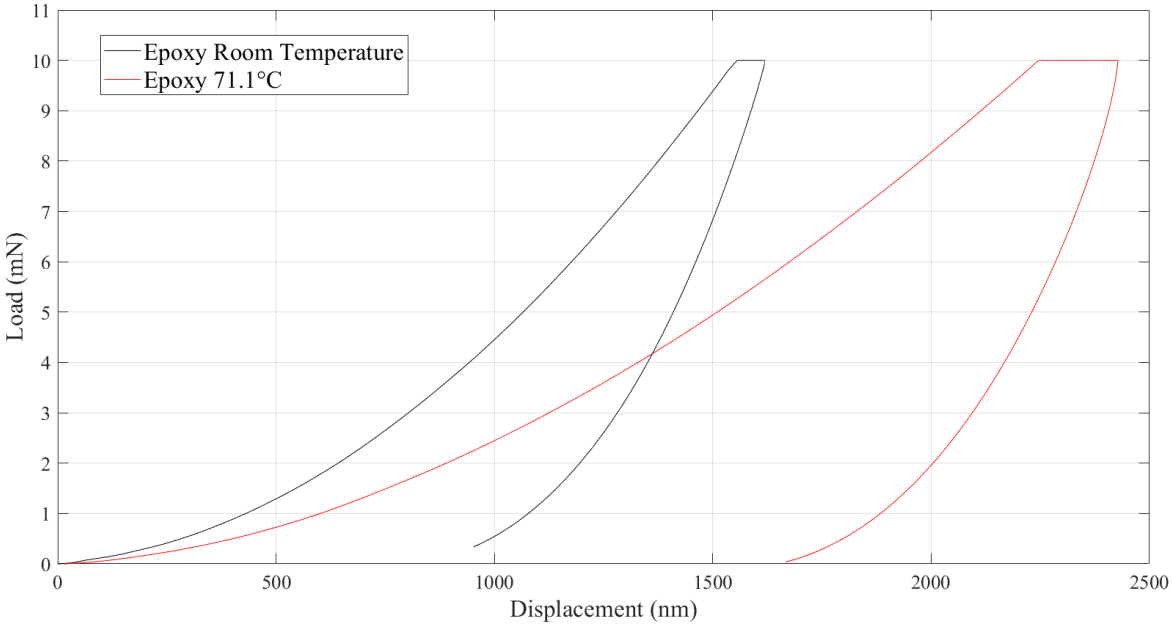

Figure 4.20 Epoxy xSol Comparison

Table 4.2 Comparison of Indentation Data at Elevated Temperature

	xSol Max Displacement (nm)	xSol Residual Displacement (nm)	xSol Area Between Curve (nm*mN)
As-Is Fiber	495.8	64.5	3634
ZnO Fiber	468.5	82.7	3289
MOF Fiber	481.9	66.9	3567
Aeropoxy	2427	1666	12435

SPM scans for the xSol fibers also show the indent on the surface of the fiber; the epoxy was not imaged due to its softening interfering with the scan. These images are shown in Figure 4.21. Even at elevated temperatures, there is no debonding occurring; only local sliding at the fiber/epoxy connection.

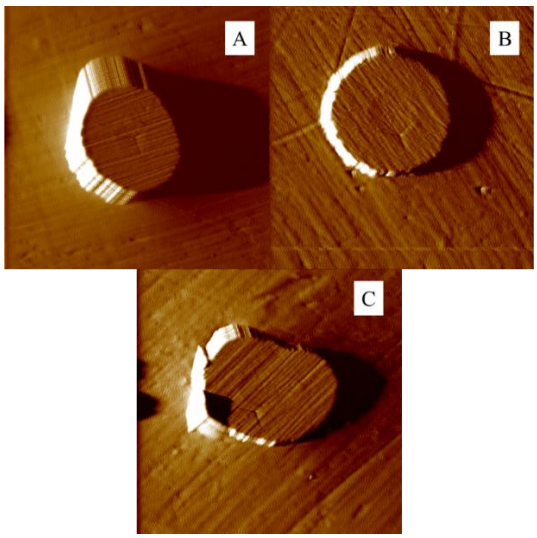

Figure 4.21 xSol SPM profiles for (a) As-Is Fiber, (b) ZnO Fiber, and (c) MOF Fiber

4.2.3 High Load Indentation

High load indentation features the same curve comparison as with low load, just at a higher loading. Figure 4.22 shows the average load-displacement curves for the high load indentations, with error bars. Each of the three curves consists of the three indents on each type of fiber. These are shown in Figure 4.23 for As-Is, Figure 4.24 for ZnO, and Figure 4.25 for MOF.

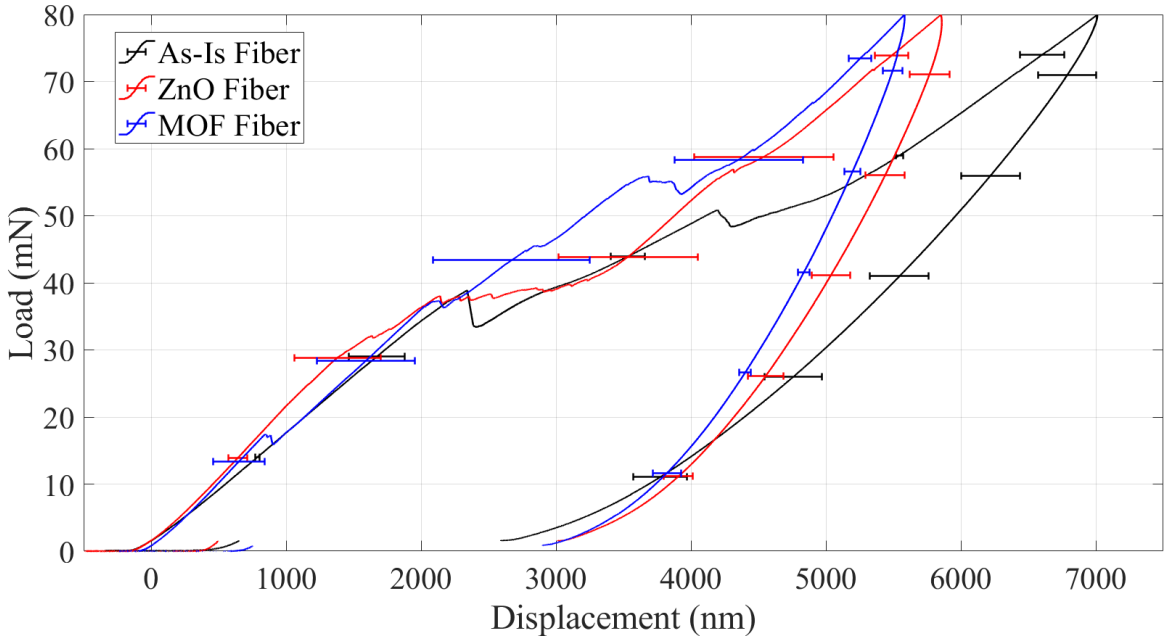

Figure 4.22 Load-Displacement Curves for High Load

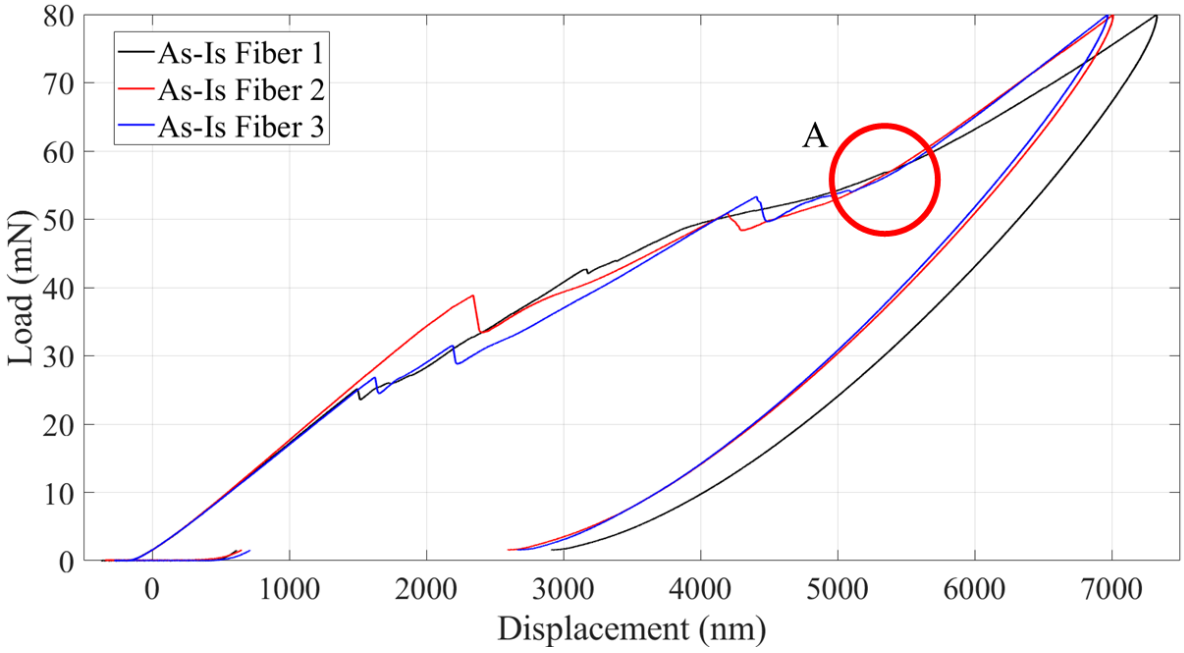

Figure 4.23 As-Is High Load Curves with Debonding Loads Highlighted

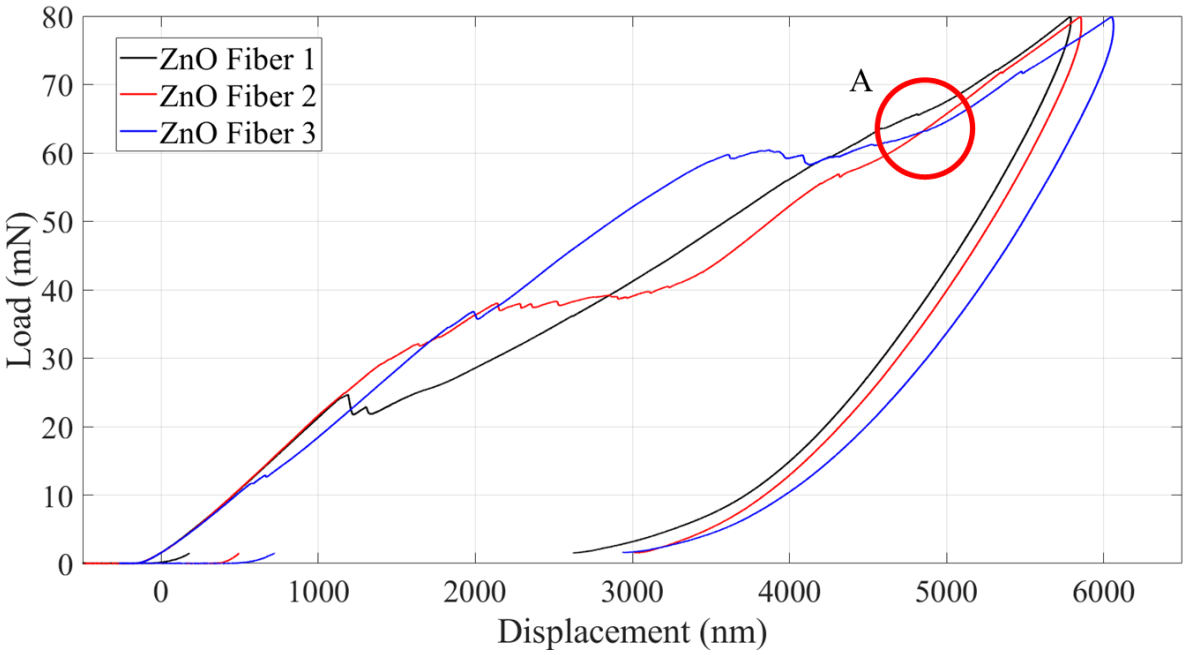

Figure 4.24 ZnO High Load Curves with Debonding Loads Highlighted

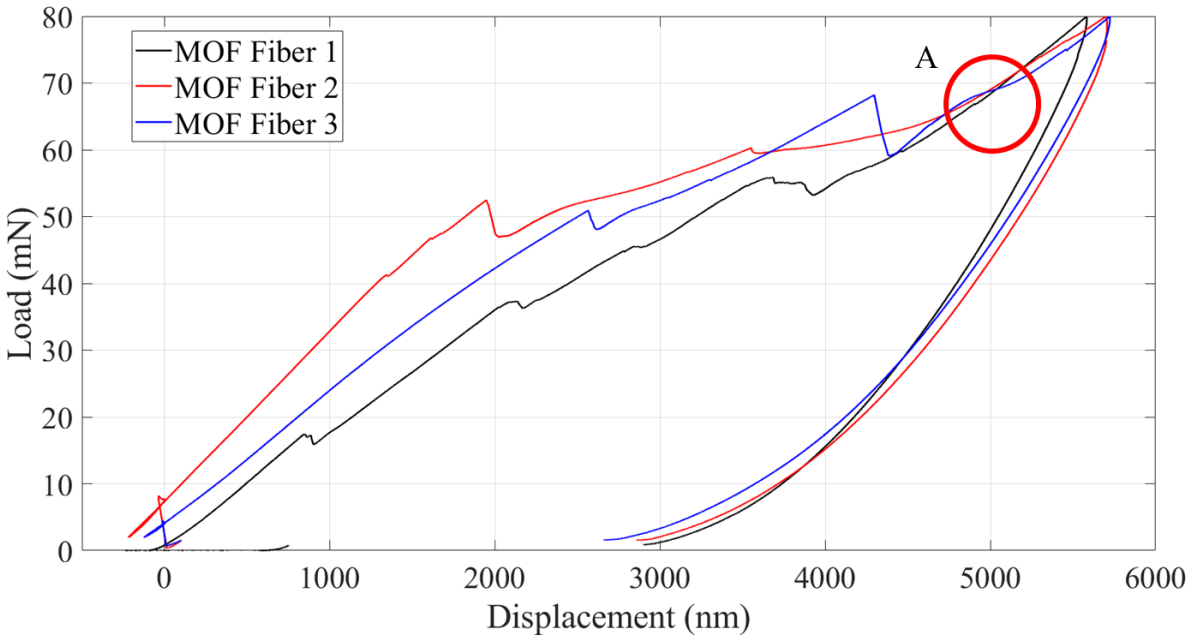

Figure 4.25 MOF High Load Curves with Debonding Highlighted

As seen in Figure 4.22, the As-Is fiber displaces the most, followed by the ZnO and MOF. Residual displacements are all around 3000 nm, but that is to be expected as the high load allows for total debonding. However, there are a couple of nonlinearities to understand first to figure out which one belongs to the debonding load. One nonlinearity occurs around 40 mN, marked by sharp jumps in the data and a "mouse ears" geometry, then another nonlinearity occurs later on; this nonlinearity is a smooth transition from linear to a nonlinear shape. To investigate which of the two nonlinearities shows debonding, a simple test is done by indenting a fiber from 15 to 40 mN, imaging each indent to see what occurs. The results of the test are shown in Figure 4.26.

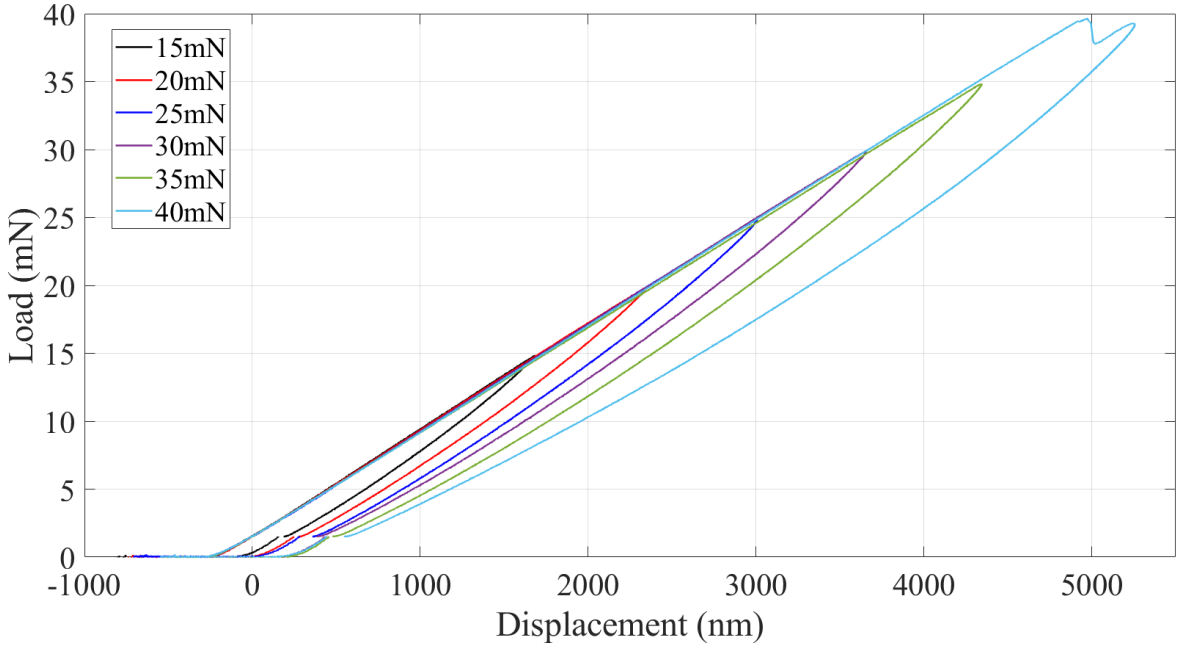

Figure 4.26 Results of Increasing Load Experiment

Figure 4.27 shows the SPM scans of the indents at 15, 30, and 40 mN. The load-displacement plots in Figure 4.26 show that the loads up to 40 mN do not result in any nonlinearities. The behavior of each of the prior 5 curves is the same, just with increasing values. However, at 40 mN, there is a discontinuity in the curve. This is corroborated with Figure 4.27c, where the scan shows

the surrounding matrix being deformed by the tip, taking the form of the “mouse ears”. Figure 4.28 helps explain why there is a nonlinearity in the load-displacement plots around 40 mN.

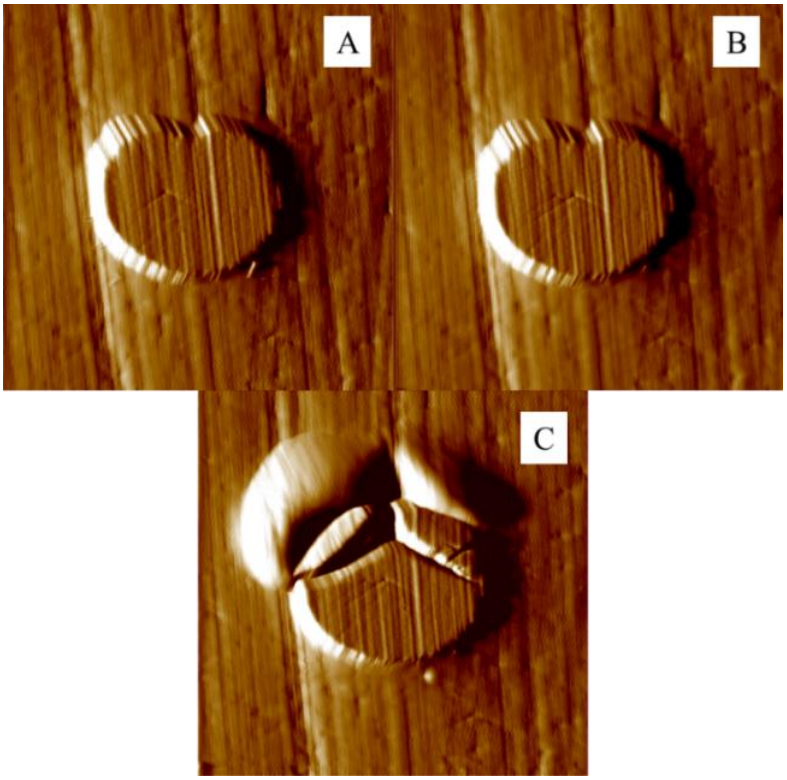

Figure 4.27 SPM Scans of (a) 15 mN, (b) 30 mN, (c) 40 mN

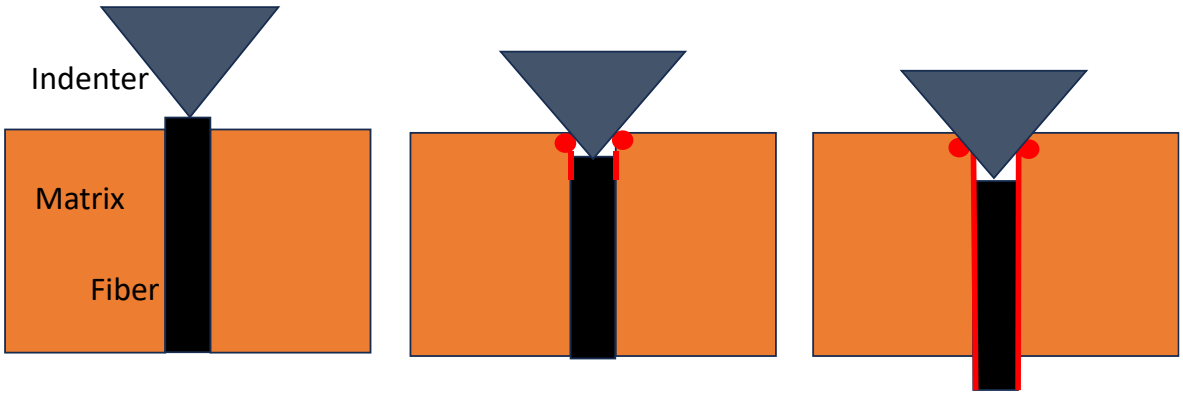

Figure 4.28 Schematic of High Load Indentation

In the leftmost image, the initial condition is shown. The fiber is slightly protruding from the surface, with the tip beginning the indentation. Then, the middle image occurs. There is some local debonding occurring in the fiber, but the main deformation occurs in the matrix. Since the high load indenter tip is slightly larger than the fiber (~10 μm compared to 7 μm), the sides of the tip begin to push the matrix out of the way, with the fiber being broken open on occasion. This is what creates the initial nonlinearity around 40 mN. Then, as the tip continues to push the fiber, the fiber completely debonds, leading to the second nonlinearity. The debonding is not a sudden failure, so there is no large jog; rather, the debonding is seen by a change in the linearity of the curve.

In Figure 4.23, Figure 4.24, and Figure 4.25, these debonding loads are denoted by the red circle. As shown in the figures, the debonding load is not as apparent as the mouse ears/fiber breakage nonlinearity as the debonding would only cause the fiber to slide. Therefore, the debonding is shown as the change in slope from linear to more quadratic. For As-Is fibers, this load occurs around 50 mN, for ZnO fibers debonding occurs at around 60 mN, and for MOF fibers the debonding occurs at around 62 mN.

To find the interfacial shear strength, the following Equation 4.1 is used. In this equation, P is the debonding load, D is the diameter of the fiber, and t is the sample thickness.

$$\tau = \frac{P}{\pi D t} \tag{4.1}$$

In this case, D is 7 μm for all the three fibers. This is because the modifications increase the size of the interface, so the fiber diameter still remains the same. The thickness of the sample is 1 cm, and the load depends on the curve. The P value for each fiber was chosen by finding the approximate point on the curve where the slope begins to change. The results of the analysis are tabulated in Table 4.3. From the table, it is clear that the interface modifications positively affect

the interfacial shear strength, increasing it by 15-20%. The MOF has a greater effect on shear strength than ZnO, owing to its slightly larger debonding load.

Table 4.3 High Load Interfacial Strength Data

Fiber Type	Debonding Load (mN)	Average Debonding Load (mN)	Interfacial Shear Strength (MPa)	Nominal Increase (%)
As-Is Fibers	51.29	51.81±1.3	2.356 ± 0.05	-
	50.84			
	53.29			
ZnO Fibers	63.62	60.10±3.3	2.733 ± 0.15	16.0
	56.95			
	59.74			
MOF Fibers	55.90	61.48±6.2	2.796 ± 0.28	18.7
	60.33			
	68.21			

4.2.4 Modulus Mapping

Figure 4.29 shows the results of modulus mapping on each of the three fibers. While the mapping collects all variables, the only ones of interest are the topology and moduli. These images show roughly circular fibers surrounded by a mostly flat plane of epoxy. The benefit of modulus mapping shows itself on the second and third rows. Looking at storage and loss moduli, there is a clear distinction between the fiber and epoxy; the epoxy data is a dark brown, while the fiber data is a brighter brown/white. Here, the interface region is in the small transition region between the fiber and epoxy. To explore this further, a profile of the storage and loss modulus is created. This profile looks at the variable of interest along the distance of the line. Profiles are chosen on each fiber such that the noise is minimized. The profile comparisons of each modulus are shown in Figure 4.30, with length scales calibrated using similar SEM images.

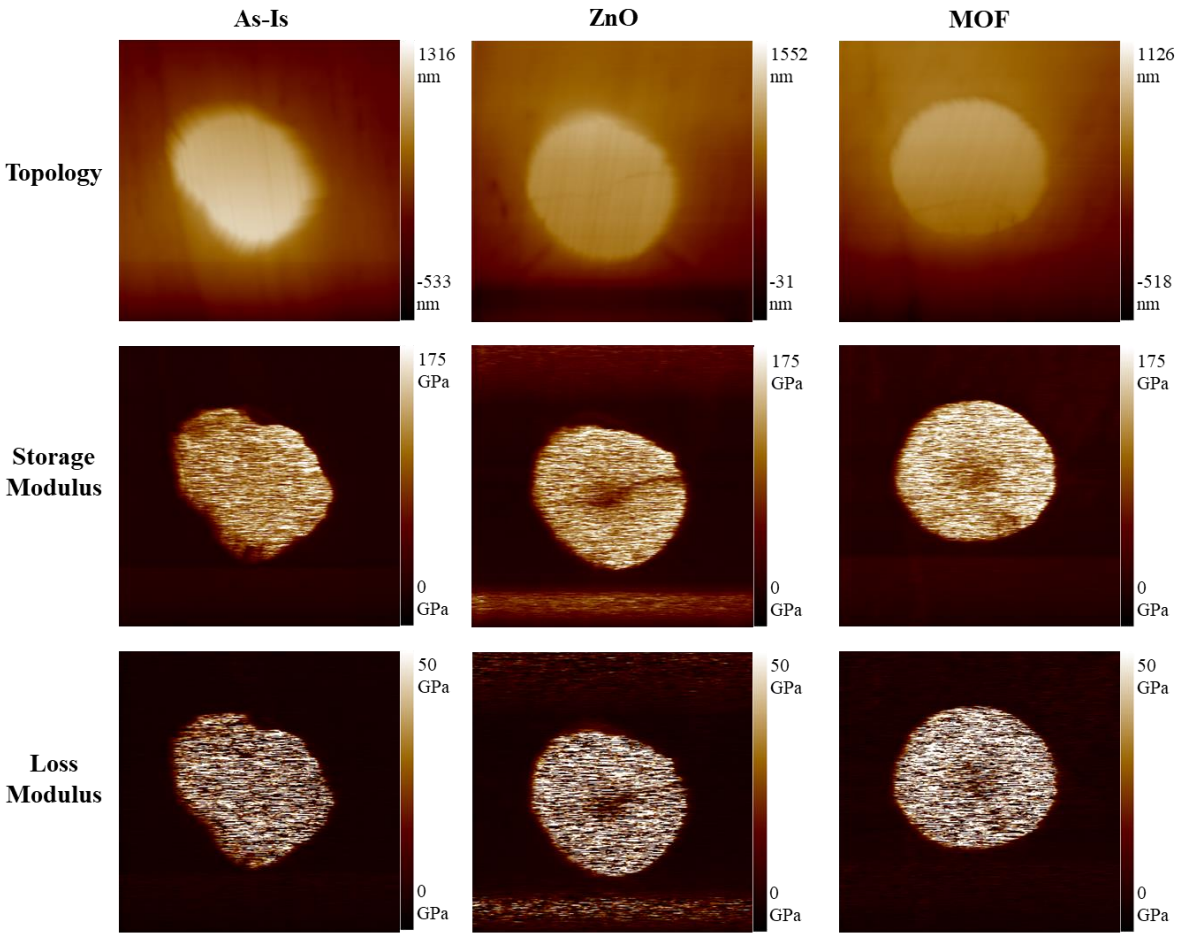

Figure 4.29 Modulus Mapping Results Showing Topology (top row), Storage Modulus (middle row), and Loss Modulus (bottom row) for each fiber

The profile plots in Figure 4.30 support the scans, showing a clear transition region fiber and matrix properties, around 3 and 10 μm. As the modulus map process uses a low load and results in small indentation depths, there is a lot of y-axis data noise in the modulus profiles on the significantly harder fiber than with the softer epoxy. However, the behavior of the profiles matches is similar to other modulus map studies [56]. The average moduli of both the fiber and epoxy can be found using peaks and valleys. This averaging shows that the storage modulus of carbon fiber is 121.5±9.832 GPa and 20.89±3.761 GPa for the epoxy. The loss modulus of the fiber is 19.44±3.882 GPa and 2.280±0.297 GPa for the epoxy. The interior of the carbon fiber is not

affected by the surface modifications, so the variation peaks and valleys in each fiber type is attributed to the low load noise. Essentially, the spread of data is within the margin of error. The interface region is looked into further by taking a snapshot of the transition region going from the epoxy to the fiber.

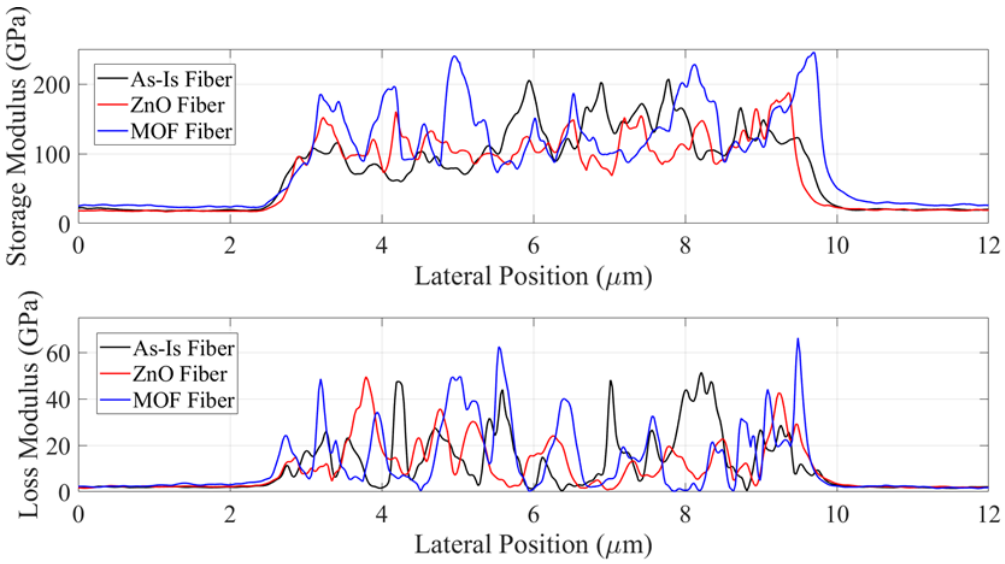

Figure 4.30 (a) Storage Modulus Profiles. (b) Loss Modulus Profiles

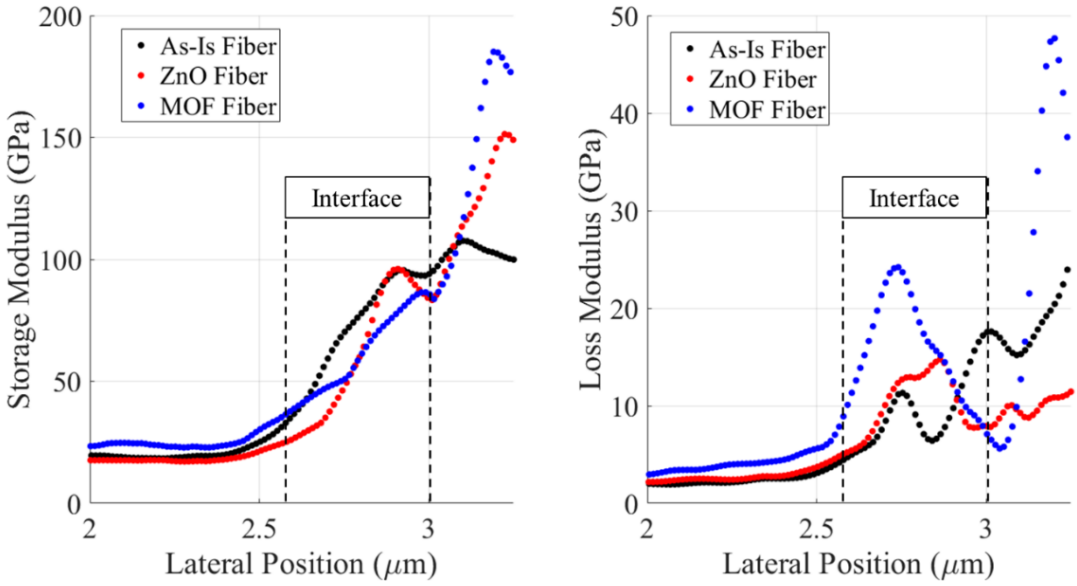

Figure 4.31 Snapshot of Matrix-Fiber Transition Region

Figure 4.31 shows a snapshot of the transition region from matrix to fiber. Looking at the profile, the interface seems to be from 2.6 μm to 3 μm. Inside this region, the storage modulus is analyzed. The As-Is fiber modulus essentially linearly increases from the matrix to the fiber. The ZnO profile in red shows a much sharper increase to a maximum, then going to the fiber properties. Finally, the MOF curve in blue has a moderate increase, with a small nonlinearity just before the fiber. The sharp increase of ZnO near the fiber can be attributed to the ZnO nanorods acting as a cantilever beam that is fixed to the fiber. From the small size of the MOF, it would not lead to a big change in the curve, so the slight nonlinearity near the 2.75 μm mark may be the beginning of the MOF, ending around 3 μm. It is interesting that the ZnO nanorods have a larger effect in modulus mapping, when the MOF has a greater interfacial strength. This may be due to the cantilever beam effect of the ZnO on the fiber. For MOF, the effect is slight in the change in slope after the 2.75 μm point, where the 2 curves have different slopes. This is also seen in the loss modulus curve where the MOF curve increases to its maximum around 2.75 μm, then decreasing sharply.

4.3 Wetting Considerations

A different way to look at the interfacial behavior is through a chemical and hydrodynamic lens. The easiest explanation chemically is that bare carbon fibers are inert and would not attract the epoxy any more than the basic van der Waals forces that usually exist, but the nano-species would be different. They are grown in functional groups and are themselves non-inert. This would immediately strengthen the bonding between the epoxy and fiber, as well as have a better attraction with the epoxy. The porous structure of MOF would also give the epoxy more surface area to promote chemical interactions. Two hydrodynamics models are well known in literature that elucidate what is occurring in the interface. For non-ideal surfaces, the two models are the Wenzel and the Cassie-Baxter models [68], shown pictorially in Figure 4.32.

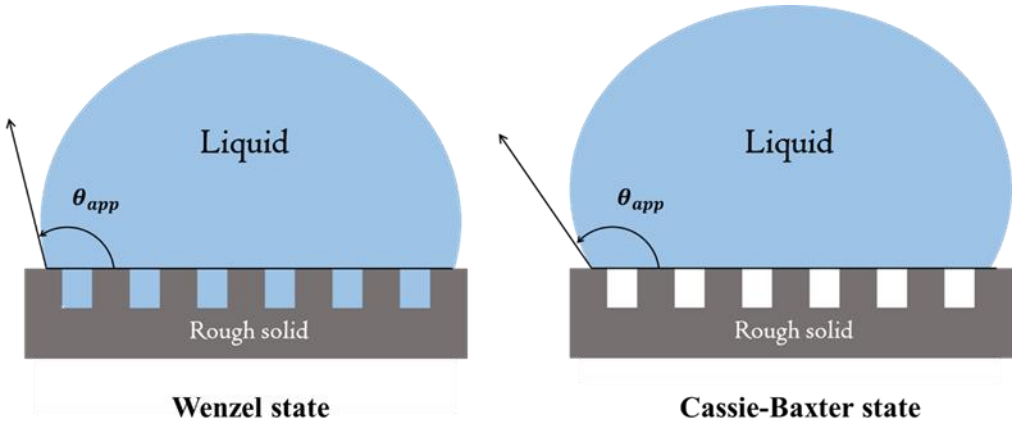

Figure 4.32 Schematic of Wenzel and Cassie-Baxter Wetting Models

In a Wenzel state (left of Figure 4.32), the liquid will wet the entire surface including any nonlinearities where it can be assumed that the nano-species are nonlinearities. The variable θ_{app} is the apparent contact angle of a liquid drop (in this case epoxy); this is defined as the equilibrium contact angle times a roughness factor. An equilibrium angle less than 90° would imply a wetting pair between solid and liquid, and an angle greater than 90° indicates a non-wetting pair. From this model, it is clear that a wetting solid surface would become more wet if made rougher as the liquid would sink between the pores more, leading to a lower equilibrium angle. On the other hand, a non-wetting surface would be made more non-wetting, as the angle would increase. Therefore, creating more topological roughness on the solid (carbon fiber) surface would amplify the wetting behavior of the epoxy with the Wenzel state.

In the Cassie-Baxter wetting state (right of Figure 4.32), the pores formed by the nonlinearities are not initially wetted, rather holding air pockets. In this model, the apparent contact angle is found using an area average of the individual types of microscopic regions of note; in this case, the fiber and the nano-species. Given the two materials 1 and 2 having their own contact angle θ and area fraction f, the apparent contact angle is given as Equation 4.2.

$$\cos(\theta_{app}) = f_1 \cos(\theta_1) + f_2 \cos(\theta_2) \quad (4.2)$$

From this equation, it is clear that the Cassie-Baxter model predicts that a smooth wetting surface (carbon fiber) can be made more wet if some nonlinearity (nano-species) is introduced that has better wetting properties (such as surface energy) than the initial surface. In terms of the modified carbon fibers, the nanostructures in this study have higher surface energies than carbon fibers [69]. Based on this, it is clear that regardless of which model the epoxy-fiber system behaves in, the presence of nanostructures on the surface of the fiber will increase the epoxy wetting on the fiber's surface.

Another consideration is wetting timescale. This is a critical parameter as the epoxy should be wetting the surface of the fiber in a timeframe sooner than the curing timeframe. If wetting takes longer than curing, the interface will be weak. On the other hand, if wetting time is faster than curing time, the interface will benefit from the enhanced surface area from the nanoscale modifications, resulting in a strong interface and increased interfacial shear strength. Looking at wetting parameters, it stands to reason that the increased surface energy of the nano-species will result in faster wetting times than with bare fibers, resulting in stronger interfaces. This is another reason the modified carbon fibers have higher interfacial shear strengths than the As-Is carbon fibers.

4.4 Discussion

The physical effect of the nano-species in this study is clearly shown from the beginning with the SEM imaging. Looking at the change from bare fiber, ZnO takes on the form of small cantilever beams. They are quite large at almost 1 μm in diameter and about 2 μm in length using this growth method. Most importantly, they are not in a uniform pattern, spread out at various angles and orientations. This would result in a "Velcro" type behavior, leading to that effective mechanical

tethering seen in the indentation results. While the epoxy can seep into the cracks between each ZnO crystal, its main benefit comes from that random orientation based tethering.

On the other hand, MOF has a more sponge-like structure. This would allow for the epoxy to seep into each pore, giving the epoxy the ability to bond to both the nanostructure and the fiber. This is most likely the reason behind the MOF having better mechanical performance than ZnO. It is also apparent that the nano-species increase the surface area on the fiber. Finding the increase of ZnO is simple, as the crystals are structured as hexagonal prisms. With the SEM imaging suggesting a full 100% coverage of the fiber, and using the SEM measurements, the surface area of the carbon fiber increases by 500-550% accounting for some small variations in measurements. On the other hand, MOF is slightly harder to find the increase in area. With an assumption that the sponge structure also is slightly hexagonal, and using the SEM imaging measurements, the MOF increases surface area by 1000-1100%. There is a lot more range with MOF as the measurements can vary greatly, but generally the MOF pores are on the smaller and thinner size so smaller measurements were used. This increased surface area would benefit thermal performance as well, shown by thermal camera testing done by Kumar et al. [24]. The thermal performance increase would also benefit additive manufacturing, allowing for faster curing epoxies to be used during production.

Moving to mechanical performance, the low load indentations gave some information about the system, but nothing super meaningful. As the load was too light on the fiber, there would only be some slight local sliding where the fiber and epoxy meet, but nothing that would lead to debonding. More of the work done by the indenter would have gone into making the indentation mark on the fiber itself, which would be part of the reason all the residual displacements were about the same for each fiber and the maximum displacements were roughly similar to each other.

However, due to the local sliding effect, there is still a difference in the maximum displacement in that the ZnO and MOF had lower maximum displacements than the As-Is fibers. The addition of temperature did not have an effect on the load-displacement data; the epoxy was softened to such a degree that the experimental data would be affected more by softening of epoxy than weakening of the interface. In imaging, the epoxy was softening such that fibers would start to sink in the matrix. This is shown in the xSol epoxy comparison where the deflection and toughness doubled from room temperature. On the fiber side, the maximum displacement increased but not enough to be meaningful.

The high load indentation shows the effect of the nanoscale modification on the interfacial strength. The ZnO and MOF curves shifted to the left as compared to As-Is, suggesting here that even though there was debonding, the nano-species still resisted the sliding motion. The interfacial shear strength also increased for ZnO and MOF, with MOF having a slightly higher strength. This could be due to the difference in morphologies, as cantilever beams would be strongest very close to the fiber and debonding could have occurred further away from the surface. An interesting point is that the low load results showed ZnO with superior performance, but the high load results showed that the MOF has superior performance. This could be due to the lower load resulting in a more stiffness based result (parameter EI), wherein the ZnO modified fibers have a higher stiffness than MOF fibers. However, high load results consider not just stiffness but also interfacial adhesion. Modulus mapping also gave some insight into the behaviors occurring near the interface, but the process could be refined or more data gathered to remove the effect of noise and fibers not being flushed with the surface.

Looking at hydrodynamics, interfacial tension would give a clear picture of what is happening. The interfacial tension of ZnO-epoxy interface is 700 mNm^{-1} [70], and the tension of the MOF-

epoxy interface is 20.7 mNm^{-1} [71]. The lower the interfacial tension, the better the wetting performance would be. This would also be a reason the MOF carbon fibers performed better than ZnO fibers. Looking at surface free energy as well, the nano-species would have higher surface free energy than the bare fiber; this promotes bonding as there is more energy that the epoxy can use on the surface of the nano-species to bond to.

As explained in Sections 2.3 and 2.4, the use of nanoscale modification is more than just a mechanical benefit. Zinc oxide, for example, is a great piezoelectric material. Therefore, these nanoscale modifications can be used for both strengthening and for multi-functional composites. Studies already exist that use ZnO coated hybrid composites in energy harvesting scenarios [72]. These multi-functional composites would pave the way for future structural and material design, having both increased strength and multiple functions.

5 Conclusions and Future Work

From this research, many insights were gained from theoretical aspects of nanoscale modification to the experimental comparisons of the fibers. Microstructural characterization showed the geometries of the nano-species, with the ZnO having a large cantilever beam type structure and the MOF having a more porous structure. The low load indentation did not explicitly give any new information, rather only showing the basic effects of local deformation. The high load debonding experiments showed that the interfacial shear strength increased by 16% for ZnO nanorods and 18.67% for MOF. Modulus mapping gave a better understanding of the transition region between the fiber and matrix, further explaining the effects of the nanoscale modification. Comparing all these results and looking at interfacial tensions and other wetting parameters showed that the MOF has better performance due to its porous structure, which brings in more epoxy to the surface of the fiber than the ZnO. This results in a more complete and stronger bond. Some basic modeling was performed using a cohesive zone model but requires some further work as the parameters were not well tuned. Overall, the understanding was made that these nano-species increase the performance of the composite by having increased epoxy wetting and mechanical tethering between the fiber and epoxy. The increased surface area would also help in this manner due to there being more area for the epoxy to bond to.

5.1 Future Work

With a method for nanoscale single fiber interfacial shear strength calculation established, it can be adapted to more than just a carbon fiber/polymer matrix combination. Other methods of modification can be looked at on other fiber types like a hydroxyapatite coating on natural jute fibers. The existing modifications (ZnO and MOF) can also be attempted to be used on glass fibers or aramids. The ZnO and MOF morphologies can also be optimized for optimum performance as well, as the design of ZnO is a big factor in the interfacial performance of composites. Further

nanoindentation studies can also be performed, as the nanoindenter has other capabilities such as scratch or electrical conductivity modules. With this, experiments can be done that use a surface modification like ZnO to see how electrical conductivity changes in the interface as compared to fiber's surface and matrix. Finally, the interfacial shear strength experiments can be redone with a more optimized tip such as an accurately sized punch tip. This would be a benefit because the punch tip would remove the effect of the "mouse ears". Even an accurately sized berkovitch tip can remove that effect. From this, cleaner curves can be made that do not have that nonlinearity around 40 mN, making the point of debonding clearer without the distraction of the mouse ears nonlinearities.

In terms of modeling, wetting models can be further developed to model the behavior of epoxy on the fiber's surface. A flow model can be made for both bare and modified fibers. Furthermore, flow models can be further optimized to create geometry plots (since flow models vary based on geometry), which may allow the ability of the models to give a user what the best geometrical parameters result in the best flow capabilities. Along with that, thermal curing models can be created using differential scanning calorimetry (DSC) parameters for each modification. For example, a small piece of modified fiber can be placed in the DSC crucible with the epoxy to see how the heatflow changes with the addition of the fibers. These parameters like heatflow and degree of cure can be used to create models and compare the effects of bare and modified fibers.

Modeling of the push-in tests can also be created and optimized. Initial investigations into modeling of push-in tests used ABAQUS, primarily working with cohesive zone modeling. The benefit of cohesive zone modeling is that it can model the debonding behavior of the interface without nonlinearities. However, the cohesive material properties would have to be heavily optimized in order for the load-displacement curves from ABAQUS to match with experimental

data. Results from some preliminary tests are shown below; however, they do not match the behavior shown by the experimental results. Figure 5.1 shows the vertical deformation in the system, while Figure 5.2 shows the comparison between the experimental and modeling data. Figure 5.2 shows that the cohesive properties chosen from a literature survey of T650 and Aeropoxy did not result in accurate modeling data. Future iterations of this project would use experimentally obtained variables such as the maximum traction and separation for the interface, resulting in simulations that would match experimental data.

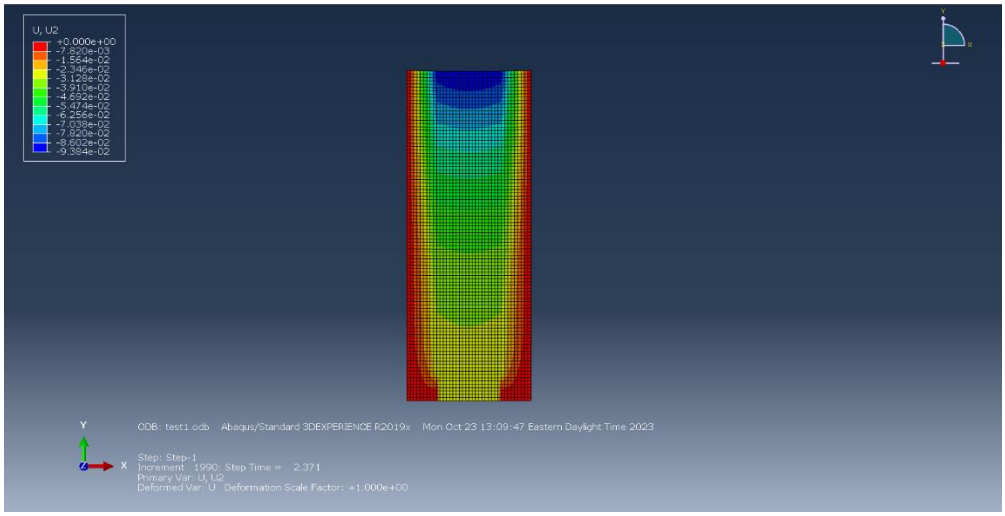

Figure 5.1 FEA Vertical Deformation Result

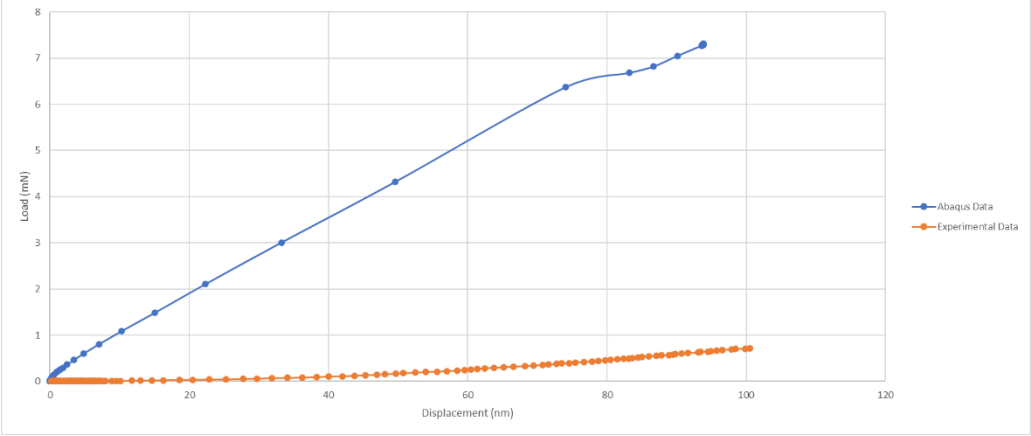

Figure 5.2 Comparison between Abaqus Data and Nanoindentation Data

6 REFERENCES

[1] Nijssen, R.P.L. "Materials," *Composite materials: an introduction*, 1st ed., Vol. 1, Inholland University of Applied Sciences, Netherlands, 2015, pp. 13.

[2] Marsh G, "Airbus takes on Boeing with reinforced plastic A350 XWB," *Reinforced Plastics*, Vol. 51, No. 11, 2007, pp. 26-27,29. https://doi.org/10.1016/S0034-3617(07)70383-1

[3] Hughes, J. D. H., "The carbon fibre/epoxy interface—A review," *Composites Science and Technology*, Vol. 41, No. 1, 1991, pp. 13-45. https://doi.org/10.1016/0266-3538(91)90050-Y

[4] Wang, H., Jin, K., Wang, C., Guo, X., Chen, Z., and Tao, J., "Effect of fiber surface functionalization on shear behavior at carbon fiber/epoxy interface through molecular dynamics analysis," *Composites Part A*, Vol. 126, 2019, pp. 105611 https://doi.org/10.1016/j.compositesa.2019.105611

[5] Piggott, M. R., "The Interface in Carbon Fibre Composites," *Carbon*, Vol. 27, No. 5, 1989, pp. 657-662. https://doi.org/10.1016/0008-6223(89)90199-1

[6] Tehrani, M., Boroujeni, A. Y., Hartman, T. B., Haugh, T. P., Case, C. W., and Al-Haik, M. S., "Mechanical characterization and impact damage assessment of a woven carbon fiber reinforced carbon nanotube–epoxy composite," *Composites Science and Technology*, Vol. 75, 2013, pp. 42-48. https://doi.org/10.1016/j.compscitech.2012.12.005

[7] Namilae, S., Li, J., and Chava, S., "Improved piezoresistivity and damage detection application of hybrid carbon nanotube sheet-graphite platelet nanocomposites," *Mechanics of Advanced Materials and Structures*, Vol. 26, No. 15, 2019, pp. 1333-1341. https://doi.org/10.1080/15376494.2018.1432812

[8] Advani, S. G., and Fan, Z., "Dispersion, Bonding and Orientation of Carbon Nanotubes in Polymer Matrices," *Processing and Properties of Nanocomposites*, published online 2006, pp. 61-98. https://doi.org/10.1142/9789812772473_0002

[9] Ma, P., Siddiqui, N. A., Marom, G., and Kim, J., "Dispersion and functionalization of carbon nanotubes for polymer-based nanocomposites: A review," *Composites Part A*, Vol. 41, No. 10, 2010, pp. 1345-1367. https://doi.org/10.1016/j.compositesa.2010.07.003

[10] Vedrtnam, A., and Sharma, S. P., "Study on the performance of different nano-species used for surface modification of carbon fiber for interface strengthening," *Composites Part A,* Vol. 125, 2019, pp. 105509.
https://doi.org/10.1016/j.compositesa.2019.105509

[11] Sharma, M., Gao, S., Mäder, E., Sharma, H., Wei, L. Y., and Bijwe, J., "Carbon fiber surfaces and composite interphases." *Composites Science and Technology*, Vol. 102, 2014, pp. 35-50.
https://doi.org/10.1016/j.compscitech.2014.07.005

[12] Tiwari, S., and Bijwe, J., "Surface Treatment of Carbon Fibers – A Review," *Procedia Technology*, Vol. 14, 2014, pp. 505-512.
https://doi.org/10.1016/j.protcy.2014.08.064

[13] Park, S., and Jang, Y., "Interfacial Characteristics and Fracture Toughness of Electrolytically Ni-Plated Carbon Fiber-Reinforced Phenolic Resin Matrix Composites," *Journal of Colloid and Interface Science*, Vol. 237, No. 1, 2001, pp. 91-97.
https://doi.org/10.1006/jcis.2001.7441

[14] Qian, H., Greenhalgh, E. S., Shaffer, M. S. P., and Bismarck, A., "Carbon nanotube-based hierarchical composites: a review," *Journal of Materials Chemistry*, Vol. 20, No. 23, 2010, pp. 4751-4762.
https://doi.org/10.1039/C000041H

[15] Liu, L., Zhou, K., He, P., and Chen, T., "Synthesis and microwave absorption properties of carbon coil–carbon fiber hybrid materials," *Materials Letters*, Vol. 110, 2013, pp. 76-79.
https://doi.org/10.1016/j.matlet.2013.07.131

[16] Wang, X., Xu, T., de Andrade, M. J., Rampalli, I., Cao, D., Haque, M., Roy, S., Baughman, R. H., and Lu, H., "The Interfacial Shear Strength of Carbon Nanotube Sheet Modified Carbon Fiber Composites," *Conference Proceedings of the Society for Experimental Mechanics*, CPSEMS, Vol. 2, 2021, pp. 25-32.

[17] Sun, J., Zhao, F., Yao, Y., Jin, Z., Liu, X., and Huang, Y., "High efficient and continuous surface modification of carbon fibers with improved tensile strength and interfacial adhesion," *Applied Surface Science*, Vol. 412, 2017, pp. 424-435.
https://doi.org/10.1016/j.apsusc.2017.03.279

[18] Lu, M., Xiao, H., Liu, M., Li, X., Li, H., and Sun, L., "Improved interfacial strength of SiO2 coated carbon fiber in cement matrix," *Cement and Concrete Composites*, Vol. 91, 2018, pp. 21-28.
https://doi.org/10.1016/j.cemconcomp.2018.04.007

[19] Sharma, R., and Kar, K., "Carbon nanotube coated carbon fiber based composite filaments for luminescent bulbs," *Materials Letters*, Vol. 137, 2014, pp. 150-152. https://doi.org/10.1016/j.matlet.2014.09.003

[20] Malakooti, M. H., Patterson, B. A., Hwang, H., and Sodano, H. A., "ZnO nanowire interfaces for high strength multifunctional composites with embedded energy harvesting," *Energy & Environmental Science*, Vol. 9, No. 2, 2016, pp. 634-643. https://doi.org/10.1039/C5EE03181H

[21] Deka, B. K., Hazarika, A., Kwon, O., Kim, D., Park, Y., and Park, H. W., "Multifunctional enhancement of woven carbon fiber/ZnO nanotube-based structural supercapacitor and polyester resin-domain solid-polymer electrolytes," *Chemical Engineering Journal*, Vol 325, 2017, pp. 672-680. https://doi.org/10.1016/j.cej.2017.05.093

[22] Yuan, H., Wang, C., Zhang, S., and Lin, X., "Effect of surface modification on carbon fiber and its reinforced phenolic matrix composite," *Applied Surface Science*, Vol. 259, 2012, pp. 288-293. https://doi.org/10.1016/j.apsusc.2012.07.034

[23] Wickramasingha, Y. A., Dharmasiri, B., Randall, J. D., Yin, Y., Andersson, G. G., Nepal, D., Newman, B., Stojcevski, F., Eyckens, D. J., and Henderson, L. C., "Surface modification of carbon fiber as a protective strategy against thermal degradation," *Composites Part A*, Vol. 153, 2022, pp. 106740. https://doi.org/10.1016/j.compositesa.2021.106740

[24] Kumar, D., Dusabimana, M. C., Al-Haik, M., and Namilae, S., "Effect of nanoscale interface modification on residual stress evolution during composite processing," *Journal of Composite Materials*, Vol. 57, No. 19, 2023, pp. 2995-3011. https://doi.org/10.1177/00219983231179522

[25] Yang, J., Xiao, J., Zeng, J., Bian, L., Peng, C., and Yang, F., "Matrix modification with silane coupling agent for carbon fiber reinforced epoxy composites," *Fibers and Polymers*, Vol. 14, 2013, pp. 759-766. https://doi.org/10.1007/s12221-013-0759-2

[26] Eyckens, D. J., Demir, B., Randall, J. D., Gengenbach, T. R., Servinis, L., Walsh, T. R., and Henderson, L. C., "Using molecular entanglement as a strategy to enhance carbon fiber-epoxy composite interfaces," *Composites Science and Technology*, Vol. 196, 2020, pp. 108225. https://doi.org/10.1016/j.compscitech.2020.108225

[27] Xu, Z., Chen, L., Huang, Y., Li, J., Wu, X., Li, X., and Jiao, Y., "Wettability of carbon fibers modified by acrylic acid and interface properties of carbon fiber/epoxy," *European Polymer Journal*, Vol. 44, No. 2, 2008, pp. 494-503. https://doi.org/10.1016/j.eurpolymj.2007.11.021

[28] Zhang, Q., Liu, J., Sager, R., Dai, L., and Baur, J., "Hierarchical composites of carbon nanotubes on carbon fiber: Influence of growth condition on fiber tensile properties," *Composites Science and Technology*, Vol. 69, No. 5, 2009, pp. 595-601. https://doi.org/10.1016/j.compscitech.2008.12.002

[29] De Greef, N., Zhang, L., Magrez, A., Forró, L., Locquet, J. P., Verpoest, I., and Seo, J. W., "Direct growth of carbon nanotubes on carbon fibers: Effect of the CVD parameters on the degradation of mechanical properties of carbon fibers," *Diamond and Related Materials*, Vol. 51, 2015, pp. 39-48. https://doi.org/10.1016/j.diamond.2014.11.002

[30] Cui, J., "Zinc oxide nanowires," *Materials Characterization*, Vol. 64, 2012, pp. 43-52. https://doi.org/10.1016/j.matchar.2011.11.017

[31] Ayyagari, S., Al-Haik, M., and Rollin, V., "Mechanical and Electrical Characterization of Carbon Fiber/Bucky Paper/Zinc Oxide Hybrid Composites," *Carbon*, Vol. 4, No. 1, 2018, pp. 6. https://doi.org/10.3390/c4010006

[32] Gao, P. X., and Wang, Z. L., "Nanoarchitectures of semiconducting and piezoelectric zinc oxide," *Journal of Applied Physics*, Vol. 97, No. 4, 2005, pp. 044304. https://doi.org/10.1063/1.1847701

[33] Pietruszka, R., Witkowski, B. S., Gieraltowska, S., Caban, P., Wachnicki, L., Zielony, E., Gwozdz, K., Bieganski, P., Placzek-Popko, E., and Godlewski, M., "New efficient solar cell structures based on zinc oxide nanorods," *Solar Energy Materials and Solar Cells*, Vol. 143, 2015, pp. 99-104. https://doi.org/10.1016/j.solmat.2015.06.042

[34] Ma, Q., Wang, Y., Kong, J., Jia, H., and Wang, Z., "Controllable synthesis of hierarchical flower-like ZnO nanostructures assembled by nanosheets and its optical properties," *Superlattices and Microstructures*, Vol. 84, 2015, pp. 1-12. https://doi.org/10.1016/j.spmi.2015.03.068

[35] Djurišić, A. B., Chen, X., Leung, Y. H., and Ng, A. M. C., "ZnO nanostructures: growth, properties and applications," *Journal of Materials Chemistry*, Vol. 22, No. 14, 2012, pp. 6526-6535. https://doi.org/10.1039/C2JM15548F

[36] Jingyu, W., Binbin, W., Larson, P., and Yingtao, L., "Synthesis and characterization of self-assembled ZnO nanoarrays on hybrid structural fibers," *Surfaces and Interfaces*, Vol. 16, 2019, pp. 188-193. https://doi.org/10.1016/j.surfin.2018.10.006

[37] Xie, F., Hu, W., Ning, D., Zhou, L., Deng, J., and Lu, Z., "ZnO nanowires decoration on carbon fiber via hydrothermal synthesis for paper-based friction materials with improved friction and wear properties," *Ceramics International*, Vol. 44, No. 4, 2018, pp. 4204-4210. https://doi.org/10.1016/j.ceramint.2017.11.224

[38] Galan, U., Lin, Y., Ehlert, G. J., and Sodano, H. A., "Effect of ZnO nanowire morphology on the interfacial strength of nanowire coated carbon fibers," *Composites Science and Technology*, Vol. 71, No. 7, 2011, pp. 946-954. https://doi.org/10.1016/j.compscitech.2011.02.010

[39] Furukawa, H., Cordova, K. E., O'Keefe, M., and Yaghi, O. M., "The Chemistry and Applications of Metal-Organic Frameworks," *Science*, Vol. 341, No. 6149, 2013, pp. 1230444. https://doi.org/10.1126/science.1230444

[40] Jiao, L., Seow, J. Y. R., Skinner, W. S., Wang, Z. U., and Jiang, H., "Metal–organic frameworks: Structures and functional applications," *Materials Today*, Vol. 27, 2019, pp. 43-68. https://doi.org/10.1016/j.mattod.2018.10.038

[41] Li, N., Zhou, L., Jin, X., Owens, G., and Chen, Z., "Simultaneous removal of tetracycline and oxytetracycline antibiotics from wastewater using a ZIF-8 metal organic-framework," *Journal of Hazardous Materials*, Vol. 366, 2019, pp. 563-572. https://doi.org/10.1016/j.jhazmat.2018.12.047

[42] Li, Y., Li, Q., Zhao, S., Chen, C., Zhou, J., Tao, K., and Han, L., "Conductive 2D Metal-Organic Frameworks Decorated on Layered Double Hydroxides Nanoflower Surface for High-Performance Supercapacitor," *Chemistry Select*, Vol. 3, No. 48, 2018, pp. 13596-13602. https://doi.org/10.1002/slct.201803150

[43] Safaei, M., Foroughi, M. M., Ebrahimpoor, N., Jahani, S., Omidi, A., and Khatami, M., "A review on metal-organic frameworks: Synthesis and applications," *TrAc Trends in Analytical Chemistry*, Vol. 118, 2019, pp. 401-425. https://doi.org/10.1016/j.trac.2019.06.007

[44] Armstrong, M. R., Shan, B., and Mu, B., "Microscopy Study of Morphology of Electrospun Fiber-MOF Composites with Secondary Growth," *MRS Advances*, Vol. 2, No. 46, 2018, pp. 2457-2463. https://doi.org/10.1557/adv.2017.413

[45] Lin, J., Wang, K., Li, J., Yang, D., Zhu, Y., and Wang, X., "Growing metal–organic framework nanoparticles on short carbon fibers to improve flame retardancy, smoke suppression and mechanical properties of the flame retardant epoxy composites," *Journal of Materials Science*, Vol. 43, 2021, pp. 19899-19914. https://doi.org/10.1007/s10853-021-06507-8

[46] Li, Y., Xie, H., Li, J., Yamauchi, Y., and Henzie, J., "Metal–Organic Framework-Derived CoOx/Carbon Composite Array for High-Performance Supercapacitors," *ACS Applied Materials & Interfaces*, Vol. 13, No. 35, 2021, pp. 41649-41656. https://doi.org/10.1021/acsami.1c10998

[47] Ayyagari, S., Al-Haik, M., Ren, Y., Abbott, A., Trigg, E. B., Zheng, B., and Koerner, H., "Metal organic frameworks modification of carbon fiber composite interface," *Composites Part B*, Vol. 224, 2021, pp. 109197. https://doi.org/10.1016/j.compositesb.2021.109197

[48] Huang, S., Fu, Q., Yan, L., and Kasal, B., "Characterization of interfacial properties between fibre and polymer matrix in composite materials – A critical review," *Journal of Materials Research and Technology*, Vol. 13, 2021, pp. 1441-1484. https://doi.org/10.1016/j.jmrt.2021.05.076

[49] Fougere, G. E., Riester, L., Ferber, M., Weertman, J. R., and Siegel, R. W., "Young's modulus of nanocrystalline Fe measured by nanoindentation," *Materials Science and Engineering: A*, Vol. 204, No. 1-2, 1995, pp. 1-6. https://doi.org/10.1016/0921-5093(95)09927-1

[50] Gregory, J. R., and Spearing, S. M., "Nanoindentation of neat and *in situ* polymers in polymer–matrix composites," *Composites Science and Technology*, Vol. 65, No. 3-4, 2005, pp. 595-607. https://doi.org/10.1016/j.compscitech.2004.09.001

[51] Wang, H. F., Nelson, J. C., Gerberich, W. W., and Deve, H. E., "Evaluation of *in situ* mechanical properties of composites by using nanoindentation techniques," *Acta Metallurgica et Materialia*, Vol. 42, No. 3, 1994, pp. 695-700. https://doi.org/10.1016/0956-7151(94)90267-4

[52] Enrique-Jiminez, P, Quiles-Díaz, S., Salavagione, H. J., Fernández-Blázquez, J. P., Monclús, M. A., Guzman de Villoria, R., Gómez-Fatou, M. A., Ania, F., and Flores, A., "Nanoindentation mapping of multiscale composites of graphene-reinforced polypropylene and carbon fibres," *Composites Science and Technology*, Vol. 169, 2019, pp. 151-157. https://doi.org/10.1016/j.compscitech.2018.11.009

[53] Randall, N. X., Vandamme, M., and Ulm, F. J., "Nanoindentation analysis as a two-dimensional tool for mapping the mechanical properties of complex surfaces," *Journal of Material Research*, Vol. 24, No. 3, 2009, pp. 679-690. https://doi.org/10.1557/jmr.2009.0149

[54] Zlotnikov, I., Zolotoyabko, E., and Fratzl, P., "Nano-scale modulus mapping of biological composite materials: Theory and practice," *Progress in Materials Science*, Vol. 87, 2017, pp. 292-320.
https://doi.org/10.1016/j.pmatsci.2017.03.002

[55] Syed Asif, S. A., Wahl, K. J., Colton, R. J., and Warren, O. L., "Quantitative imaging of nanoscale mechanical properties using hybrid nanoindentation and force modulation," *Journal of Applied Physics*, Vol. 90, No. 3, 2001, pp. 1192-1200.
https://doi.org/10.1063/1.1380218

[56] Hu, Y., Li, M., Wang, J., and Zhang, Z., "Characterization of the interphase in carbon fiber/polymer composites using a nanoscale dynamic mechanical imaging technique," *Carbon*, Vol. 48, No. 11, 2010, pp. 3229-3235.
https://doi.org/10.1016/j.carbon.2010.05.008

[57] Nishikawa, M., Okabe, T., Hemmi, K., and Takeda, N., "Micromechanical modeling of the microbond test to quantify the interfacial properties of fiber-reinforced composites," *International Journal of Solids and Structures*, Vol. 45, No. 14-15, 2008, pp. 4098-4113.
https://doi.org/10.1016/j.ijsolstr.2008.02.021

[58] Feih, S., Wonsyld, K., Minzari, D., Westermann, P., and Lilholt, H., "Establishing a Testing Procedure for the Single Fiber Fragmentation Test," *Risoe National Laboratory*, 2004, pp. 1-30.

[59] Hinoki, T., Zhang, W., Kohyama, A., Sato, S., and Noda, T., "Effect of fiber coating on interfacial shear strength of SiC/SiC by nano-indentation technique," *Journal of Nuclear Materials*, Vol. 258-263, No. 2, 1998, pp. 1567-1571.
https://doi.org/10.1016/S0022-3115(98)00220-7

[60] Rodríguez, M., Molina-Aldareguía, J. M., González, C., and LLorca, J., "A methodology to measure the interface shear strength by means of the fiber push-in test," *Composites Science and Technology*, Vol. 72, No. 15, 2012, pp. 1924-1932.
https://doi.org/10.1016/j.compscitech.2012.08.011

[61] Rohrmüller, B., Gumbsch, P., and Hohe, J., "Calibrating a fiber–matrix interface failure model to single fiber push-out tests and numerical simulations," *Composites Part A*, Vol. 150, 2021, pp. 106607.
https://doi.org/10.1016/j.compositesa.2021.106607

[62] Chen, X., Wen, K., Wang, C., Cheng, S., Wang, S., Ma, H., Tian, H., Zhang, J., Li, X., and Shao, J., "Enhancing mechanical strength of carbon fiber-epoxy interface through electrowetting of fiber surface," *Composites Part B*, Vol. 234, 2022, pp. 109751.
https://doi.org/10.1016/j.compositesb.2022.109751

[63] Sathyanath, R., and Kalpathy, S. K., "Morphological features and dewetting behaviour of thin polymer films coated on porous substrates," *Materials Today: Proceedings*, Vol. 44, No. 2, 2021, pp. 2939-2944.
https://doi.org/10.1016/j.matpr.2021.01.929

[64] Namilae, S., and Minguet, P., "Study of Fracture Process Zone Characteristics Using Cohesive Zone Models," *Boeing Technical Journal*, Vol. 3, No. 1, 2013.

[65] Li, X., Yang, Q., and Liu Z., "Interfacial mechanics of fiber push-out test: nano-indention technique and cohesive element modeling," *13th International Conference on Fracture*, Beijing, China, June 2013, pp. 1-7.

[66] Xu, T., Luo, H., Xu, Z., Hu, Z., Minary-Jolandan, M., Roy, S., and Lu, H., "Evaluation of the Effect of Thermal Oxidation and Moisture on the Interfacial Shear Strength of Unidirectional IM7/BMI Composite by Fiber Push-in Nanoindentation," *Experimental Mechanics*, Vol. 58, 2018, pp. 111-123.
https://doi.org/10.1007/s11340-017-0335-6

[67] "THORNEL T-650/35 PAN-BASED FIBER," Fibermax Composites, May 2012.
https://www.fibermaxcomposites.com/shop/datasheets/T650.pdf

[68] Whyman, G., Bormashenko, E., and Stein, T., "The rigorous derivation of Young, Cassie–Baxter and Wenzel equations and the analysis of the contact angle hysteresis phenomenon," *Chemical Physics Letter*, Vol. 450, No. 4-6, 2008, pp. 355-359.
https://doi.org/10.1016/j.cplett.2007.11.033

[69] Kontogeorgis, G. M., and Kill, S., *Introduction to Applied Colloid and Surface Chemistry*, 1st, Vol. 1, Wiley, New York, 2016.

[70] Na, S., Park, C., "First-Principles Study of the Surface of Wurtzite ZnO and ZnS - Implications for Nanostructure Formation," *Journal of the Korean Physical Society*, Vol. 54, No. 9, 2009, pp. 867-872.
https://doi.org/10.3938/jkps.54.867

[71] Hou, B., Song, K., Rehman, Z. U., Song, T., Lin, T., Zhang, W., Pan, Y., and Yang, R., "Precise Control of a Yolk-Double Shell Metal–Organic Framework-Based Nanostructure Provides Enhanced Fire Safety for Epoxy Nanocomposites," *ACS Applied Materials & Interfaces*, Vol. 14, No. 12, 2022, pp. 14805-14816.
https://doi.org/10.1021/acsami.2c01334

[72] Kumar, B., Kim, S., "Energy harvesting based on semiconducting piezoelectric ZnO nanostructures," *Nano Energy*, Vol. 1, No. 3, 2012, pp. 342-355.
https://doi.org/10.1016/j.nanoen.2012.02.001